
Nucleation and Crystallization of the Metastable Hard Sphere Fluid

by Wilkin Wöhler

PHYSICS - MASTER THESIS

ALBERT-LUDWIGS UNIVERSITY OF FREIBURG

MAY 2021

Elaborated within the
Research group for complex systems and soft matter

under the supervision of
Prof. Dr. Tanja Schilling

Declaration of originality

Herewith I affirm that the submitted master thesis was written autonomously by myself and that I did not use any other sources and auxiliaries than declared in this work. Under the acknowledged rules of scientific work (*lege artis*) literal or analogous content borrowed from the work of others was appropriately identified. Furthermore, I insure that the submitted master thesis is not and was never part of any other examination procedures, either complete or in substantial parts.

Freiburg, ____ . ____ . _____

Abstract

The thesis at hand studies the nucleation process of the metastable hard sphere liquid. It focuses on understanding the discrepancy between experimentally and theoretically determined nucleation rates. Regarding it, a possible solution is proposed based on a broad analysis of the process. Further, the existance of non-Markovian effects are investigated. We find a mostly featureless Gaussian memory kernel of constant width. However, a clear interpretation or relation to direct accessible quantities requires further research.

Also, key features and testing of the employed event driven molecular dynamics (EDMD) simulation code are presented as well as an analysis of the produced simulation trajectories. The analysis includes measurements of the long time self-diffusion constant, the time scale on which local ordering processes take place and the attachement rate of particles to a growing cluster. Furthermore, shape descriptors for clusters at different stages are evaluated regarding their dependence on different quantities describing the growth process. In the analysis, however, no dependence is observed.

The nucleation study is based on simulations with 2000 trajectories at $\eta \in [53.1\%, 53.4\%]$ of which each contains about one million particles. The memory kernel analysis is based on about 500 trajectories at $\eta = 54.0\%$. In this case each simulation contains 16384 particles to reach complete crystallization.

Contents

1. Introduction and theory	1
1.1. Introduction	1
1.1.1. Testing the Markovian assumption	1
1.1.2. Studying the nucleation rate discrepancy	2
1.2. The hard sphere system	3
1.3. The hard sphere phase diagram and its metastable state	3
1.4. Classical nucleation theory	7
1.5. Computer precision and chaotic behavior	9
1.6. Comparison to real world experiments	11
2. Simulation details and testing	13
2.1. Algorithm and simulation details	13
2.1.1. Event driven molecular dynamics (EDMD)	14
2.1.2. Details concerning the implementation	16
2.1.3. The simulation periphery	22
2.2. Testing of the simulation code	23
2.2.1. Diffusive behavior	23
2.2.2. Radial distribution function	25
2.3. Estimate of required resources	27
2.3.1. Calculation time estimate	27
2.3.2. File sizes estimate	28
2.4. Preliminary data for equilibration test	29
2.5. Extensions for future studies	33
2.5.1. Polydispersity for varying radius and mass	33
2.5.2. Single cluster tracking algorithm	34
3. Data Analysis	37
3.1. Parameter choice of the simulated system	37
3.2. Long time diffusion time scale	38
3.3. Cluster size distribution over time	39
3.4. Autocovariance functions of largest cluster in the metastable fluid	42
3.5. Cluster growth and constant attachment rate	43

3.6. Evaluation of shape descriptors	46
3.7. The nucleation time dilemma	49
3.8. Induction time by exponential distribution assumption	51
3.8.1. CNT expectation of the induction time distribution	51
3.8.2. Maximum likelihood estimator of the induction time	52
3.8.3. Monte Carlo uncertainty estimation	54
3.9. Nucleation rate discrepancy and possible solution	56
3.9.1. Comparison to literature	56
3.9.2. Solid fraction in the thermodynamic limit of infinite volume	57
3.10. Memory kernel analysis of nucleating ensemble	59
4. Conclusion	62
A. Derivation of momentum transfer in elastic hard sphere collisions	64

List of Figures

1.3.1. Phase diagram of hard sphere fluid	5
1.4.1. Free energy difference between fluid and solid phase	8
1.4.2. Critical radius in the metastable regime	9
1.5.1. Exponential growth of perturbations in chaotic system	10
2.2.1. Long time diffusion constant at varying volume fractions	25
2.2.2. Radial distribution functions at varying volume fractions	26
2.2.3. Radial distribution function with Percus-Yevick approximation	26
2.3.1. Calculation time estimate of the simulation	27
2.3.2. Quadratic calculation time of q6q6-order parameter cluster finding routine	28
2.3.3. File size estimate of the simulation	29
2.4.1. Gaussian filter applied to cluster size distribution	30
2.4.2. Heat maps of differences under variation of equilibration step number	31
2.4.3. Heat maps of differences under variation of initial density	31
2.4.4. Nucleation rates of equilibration test measurements	32
2.5.1. Individual cluster tracking example	34
2.5.2. Example of correlation between an unstable cluster's size and lifetime	35
3.2.1. Long time self-diffusion constant measurements from production data	39
3.3.1. Cluster size distributions over time shortly after the quench	40
3.3.2. Cluster size distributions for long waiting times	41
3.4.1. Autocovariance functions of largest cluster in the metastable fluid	43
3.5.1. Largest cluster trajectories from production data with constant attachment rates	45
3.5.2. Constant attachment rate measurements from production data	45
3.6.1. Tensor of gyration measurements from production data	48
3.7.1. Comparison of different definitions for the induction time	50
3.8.1. Monte Carlo uncertainty estimation example	54
3.8.2. Nucleation rate uncertainty depending on measurement time	55
3.9.1. Nucleation rate comparison with literature values	56
3.9.2. Nucleation rate comparison under assumption of early filled boxes	58
3.10.1. Largest cluster trajectories of small system with percentiles and average	60
3.10.2. Width and amplitude of memory kernel alongside an example slice	61

List of Tables

2.1.1.	Event struct content	16
2.1.2.	Cell boundary crossing conditions	19
2.1.3.	Lookup table of cell neighbor indices	20
2.2.1.	Simulation parameters for diffusion measurement	24
2.4.1.	Simulation parameters for testing equilibration step number and initial density	30
3.1.1.	Simulation parameters of data production systems	37
3.10.1.	Simulation parameters of data production system with 16384 particles	59

1. Introduction and theory

1.1. Introduction

Understanding and describing phase transitions has always been as important as it has been challenging. On the one hand, its importance can be seen in technological disciplines like metallurgy or in scientific fields like atmosphere physics. Metal melts, for example, will form different grain sizes depending on how fast they solidify. The need for an accurate description of phase transitions then becomes obvious when considering that the grain size is crucial for properties like rigidity and brittleness. On the other hand, the challenge is due to the large number of participating particles which make an exact description impossible.

Nevertheless, a concept to qualitatively describe phase transitions was developed early on. Today, this is called classical nucleation theory (CNT). In it, a free energy is defined for some collective observable which describes the transition. This free energy landscape includes a barrier separating the two distinct phases and starting from the unfavorable phase, the system will eventually cross the barrier due to thermic Markovian fluctuations. The average duration of this process is called induction or nucleation time and usually is determined by the temperature and the barrier height.

1.1.1. Testing the Markovian assumption

In section 1.4, CNT is discussed in more detail. Also, it is used a few times within this thesis. However, it has been shown by Sear 2012[1] that in many circumstances the approach fails to provide a quantitative description. As this is not only unsatisfying for a theorist, but actually of importance in many fields of science, various approaches to solve this problem have been proposed in the past. A comprehensive list of them can be found by Kuhnbold et al. 2019[2]. The list includes modifying the free energy landscape, choosing suitable reaction coordinates or to include non-Markovian effects in the description.

In the article by Kuhnbold et al., the presence of the latter is illustrated for the largest cluster in the metastable Lennard-Jones system. Similarly Pelagejcev 2019[3] found non-negligible memory kernels in the same system by employing a numeric memory kernel reconstruction scheme

which was derived by Meyer et al. 2019[4]. In this thesis, we will continue to extend the examples of memory kernel studies by adding our findings in the elastic hard sphere system in section 3.10.

While the theory and framework to obtain the non-stationary memory kernel is too broad to cover at this point, we may mention the foundations as given by Meyer 2020[5] in his dissertation.

In the 1960's Mori and Zwanzig used their projection operator formalisms to show that memory effects can a priori not be excluded for the time evolution of collective observables. Within these formalisms, the generalized Langevin equation (GLE) was derived and later on Grabert developed a time dependent formalism to include non-stationarity. Based on these earlier works, the non-stationary generalized Langevin equation was derived by Meyer et al. 2017[6]. It is the equation of motion for a coarse grained observable A and is given by

$$\frac{dA_t}{dt} = \omega(t)A_t + \int_0^t K(\tau, t)A_\tau d\tau + \eta_{0,t}. \quad (1.1.1)$$

In the equation, A_t denotes the observable which depends on the time t for a specific trajectory, $\omega(t)$ is the time dependent friction coefficient, $\eta_{0,t}$ is the time dependent noise term and $K(\tau, t)$ is the memory kernel depending on two times. From the structure, we see that the kernel holds the information on how the observable's history influences its future. Moreover, we see that the equation is fully time dependent to suit the description of non-stationary processes like phase transitions. For purely Markovian and stationary processes, we expect to find a Dirac delta distribution, as no memory is present. In this case, eq. 1.1.1 simplifies to the usual Langevin equation.

1.1.2. Studying the nucleation rate discrepancy

While the study of memory effects is one major aim of this thesis, the other one is to measure nucleation rates of the metastable hard sphere fluid. They are an active topic of research, as those from laboratory based experiments and those from numerical simulation studies differ by orders of magnitude. See for example Auer and Frenkel 2001[7], Filion et al. 2010[8], Schilling et al. 2011[9], Wood 2019[10] or Fiorucci et al. 2020[11]. To shed some light on the problem, a detailed analysis and characterization of the nucleation process is done. This leads to a possible remedy of the discrepancy as is discussed in section 3.9.2.

1.2. The hard sphere system

The hard sphere system is the simplest model of a fluid which goes beyond the ideal gas only by including interactions between the particles in the form of an occupied volume. Its potential between particles i and j is given by

$$V(r_{ij}) = \begin{cases} \infty & r_{ij} \leq \sigma \\ 0 & r_{ij} > \sigma \end{cases}. \quad (1.2.1)$$

In this equation, $r_{ij} = |r_j - r_i|$ denotes the distance between the two particles and σ is the diameter of a hard sphere.

While the ideal gas model without pair interactions already makes it possible to derive the famous equation of state $pV = NkT$, it does not include phase transitions yet. Those can be observed when granting the particles to occupy space, in the simplest case, by defining hard spheres of the kind in eq. 1.2.1. As it is the simplest model and it is efficiently accessible for computer simulations, the hard sphere system is very well suited to study basic properties of first order phase transitions.

The first hard sphere computer simulation dates back to the beginning of electronic computer technology, in first studies by Alder and Wainwright in 1959[12]. Since then, more algorithms have been elaborated to increase efficiency and technology has advanced to a point at which virtual studies of large systems of the order of one million particles become tractable. Hence, computer simulations are becoming an even more powerful tool to study phase transitions of simple systems.

Nevertheless, even large computer simulations are very constrained in their size in comparison to laboratory based experiments, where similar systems are realizable and extensively studied. But in simulations, general properties of the system at hand can be varied effortlessly and information about each single particle can be extracted as they are naturally required. Therefore, the possibilities to analyze these virtual systems are larger than in the laboratory systems.

1.3. The hard sphere phase diagram and its metastable state

The equation of state for the monodisperse hard sphere system has various parametrizations as, for example, listed by Mulero et al. 2001[13]. The most common of them, due to its simplicity,

is the approximation proposed by Carnahan and Starling 1969[14], given by

$$Z = \frac{1 + \eta + \eta^2 - \eta^3}{(1 - \eta)^3}. \quad (1.3.1)$$

It approximates the compressibility factor Z as a function of the packing fraction η for the hard sphere fluid.

Similarly, many approximations exist for the equation of state on the stable solid branch. A common one is given by Almarza 2009[15]. It is parameterized as

$$\frac{p(v - v_0)}{k_B T} = 3 - 1.807846y + 11.56350y^2 + 141.6y^3 - 2609.26y^4 + 19328.09y^5. \quad (1.3.2)$$

In this equation, p is the pressure, v is the volume per particle, $v_0 = \sigma^3/\sqrt{2}$ is the volume per particle at close packing and $y = p\sigma^3/(k_B T)$, with k_B being the Boltzmann constant, T the temperature of the crystal and σ the diameter of the spheres.

We may note, that the inverse of the volume per particle corresponds to the number of particles per volume $v^{-1} = \rho$. The relation to the corresponding packing fraction η is given by $\rho = \frac{6}{\pi}\eta$, which can be easily shown by extending $\rho = \frac{N}{V}$ by the single particle's volume $V_s = \frac{4}{3}\pi(\frac{\sigma}{2})^3 = \frac{\pi}{6}\sigma^3$.

A first order phase transition is observed when switching between the two stable branches of the system, described by the two equations of state, between volume fractions of $\eta_{\text{freeze}} = 0.494$ and $\eta_{\text{melt}} = 0.55$. The freezing volume fraction corresponds to first solidifying clusters when approaching the transition from the liquid branch. Accordingly, the melting volume fraction indicates the melting of the crystalline phase when approaching the transition from the solid branch. Within this interval, the system tends towards a coexistence state which in equilibrium varies by the fraction of solid to liquid volume.

In detail, the liquid may follow its branch to pressures above the coexistence pressure where it becomes unstable. The particles then rearrange into the crystalline phase as each single particle can access a larger volume in the structured lattice than it would be possible in the unordered fluid.

This becomes evident by comparing the volume fractions of random close packing $\eta_{\text{RCP}} \approx 64\%$ with the one of a face centered cubic or hexagonal close packing fraction of $\eta_{\text{HCP}} \approx 74\%$. Within the crystalline phase each particle still has free accessible volume, while the randomly packed particles are already confined at exactly one place.

The additional accessible volume translates into a larger number of possible states for the particle or in terms of thermodynamics, a larger entropy which acts as a driving force for the phase transition. As the particles in the crystal are packed more densely with a volume fraction of

$\eta_{\text{melt}} = 0.55$, the pressure is reduced and not all fluid transforms into the solid phase, but both phases may coexist.

The overall phase diagram is shown with the coexistence pressure in fig. 1.3.1.

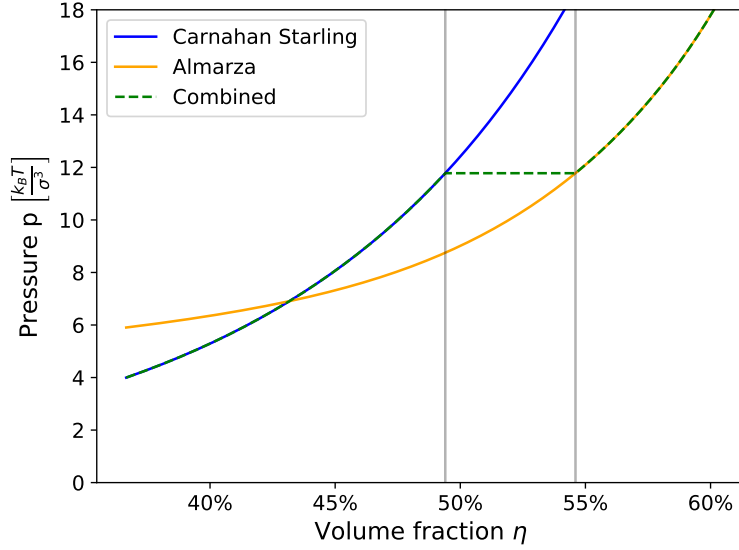


Figure 1.3.1.: Phase diagram of the hard sphere system with freezing and melting volume fraction shown as shaded lines and the green dashed line indicating the equilibrium stable branch. Where liquid and solid branch do not coincide with the stable branch, systems are unstable and tend towards a state on the stable branch.

The equilibration solid fraction of the system, $x_s = \frac{V_s}{V}$ with V_s the solid volume and V the total volume, are described by eq. 1.3.6.

For the derivation it is necessary to keep in mind that, in the stationary coexistence state, the density of the solid phase is given by the melting density and that the liquid density is equal to the freezing density, i.e $\rho_s = \rho_{\text{melt}}$ and $\rho_l = \rho_{\text{freeze}}$ respectively. When further using the trivial equations

$$\begin{aligned} V &= V_s + V_l , \\ N &= n_s + n_l , \\ N_i &= \rho_i V_i , \end{aligned} \tag{1.3.3}$$

with $n_{s/l}$ the number of solid/liquid particles we may write

$$\rho V = \rho_s V_s + \rho_l V_l . \tag{1.3.4}$$

Under the assumption of equilibrium it leads, within a few lines of calculation, to

$$\frac{V_s}{V} = \frac{\rho - \rho_{\text{freeze}}}{\rho_{\text{melt}} - \rho_{\text{freeze}}} . \quad (1.3.5)$$

As the solid fraction below ρ_{freeze} vanishes and above ρ_{melt} is 1, we can conclude that the equilibrium solid fraction of the system is given by eq. 1.3.6.

$$x_s(\rho) = \begin{cases} 0 & \rho < \rho_{\text{freeze}} \\ \frac{\rho - \rho_{\text{freeze}}}{\rho_{\text{melt}} - \rho_{\text{freeze}}} & \rho_{\text{freeze}} < \rho < \rho_{\text{melt}} \\ 1 & \rho > \rho_{\text{melt}} \end{cases} . \quad (1.3.6)$$

Evaluating eq. 1.3.6, between volume fractions of $\eta \in [0.53, 0.55]$, leads to coexistence fractions of $x_s \in [0.7, 1]$. This means that we are expecting nucleated systems in simulations to consist mostly of the solid phase after enough time for complete crystallization.

As pointed out earlier, the phase transition takes place as it reduces the pressure in the liquid. This means that already during the growth of clusters the volume fraction of the metastable liquid is reduced, potentially altering its behavior significantly. For closer inspection of this, the particle density of the metastable liquid depending on the solid fraction x_s is evaluated in eq. 1.3.9. For this purpose, first, the liquid volume V_l and the number of liquid particles N_l are expressed in terms of the solid fraction x_s :

$$V_l(x_s) = V(1 - x_s) \quad (1.3.7)$$

$$N_l(x_s) = N - n_s(x_s) = N - \rho_m V x_s = N(1 - \frac{\rho_m}{\rho} x_s) \quad (1.3.8)$$

Combining eq. 1.3.7 and eq. 1.3.8 to the expression for the particle density in the remaining liquid leads to

$$\rho_l(x_s) = \frac{N_l(x_s)}{V_l(x_s)} = \frac{N}{V} \frac{1 - \frac{\rho_m}{\rho} x_s}{1 - x_s} = \rho \frac{1 - \frac{\rho_m}{\rho} x_s}{1 - x_s} . \quad (1.3.9)$$

Evaluating the expression for relevant volume fractions within $\eta \in [53\%, 55\%]$ leads to the conclusion that crystalline fractions of $x_s < 5\%$ only reduce the packing fraction in the fluid by 0.1%. Especially for system sizes of about 1 million particles, this already corresponds to cluster sizes of a few ten thousand particles where stable growth of clusters takes place which is rather insensitive to changes of the volume fraction as shown in section 3.5. This shows, that during the highly sensitive cluster forming processes the volume fraction of the liquid can be assumed to be globally stable.

1.4. Classical nucleation theory

Classical nucleation theory (CNT) has been proposed by Becker and Döring in 1935[16] and since then used and modified multiple times to suit various types of systems. It still provides some reference or expectation, even if its framework does not seem to encompass the full nucleation process, to compare with the simulation data.

The simplest version of CNT assumes that a spherical crystallite of radius R may form in the liquid with properties of the bulk crystal, while the fluid remains with the properties of the bulk fluid. The difference in the free energy landscape is given by a surface and a volume term, each depending on the radius. The first arises from the surface tension γ between the fluid and the solid bulk phase, while the latter is caused by the difference in chemical potential $\Delta\mu$ between the two phases. The whole expression for the free energy is given by

$$\beta\Delta G(R) = 4\pi R\gamma - \frac{4}{3}\pi R^3\rho\Delta\mu, \quad (1.4.1)$$

with ρ being the particle density of the solid phase.

To calculate the difference between the chemical potentials $\Delta\mu$, we first derive the free energy difference between the metastable liquid branch and the stable coexistence branch. To calculate the free energy, we employ its differential relation

$$dF = -S dT - P dV + \mu dN. \quad (1.4.2)$$

Setting the number of particles and the temperature constant and further reformulating dV using $dN = dV\rho + V d\rho$ and $dN = 0$, we find $dV = -d\rho\frac{N}{\rho^2}$. Under this transformation, eq. 1.4.2 becomes

$$\frac{dF}{N} = \frac{P(\rho)}{\rho^2} d\rho. \quad (1.4.3)$$

The pressure $P(\rho)$ is approximated by the Carnahan-Starling equation of state where we use $\eta = \frac{6\rho}{\pi}$ and $Z = \frac{pV}{NkT} = \frac{p(\rho)}{\rho kT}$. Hence, the integration of eq. 1.4.3 between two densities $\rho_{1/2}$ is given by

$$\frac{\Delta F}{N} = \int_{\rho_1}^{\rho_2} \frac{kT}{\rho} \frac{1 + \left(\frac{6\rho}{\pi}\right) + \left(\frac{6\rho}{\pi}\right)^2 - \left(\frac{6\rho}{\pi}\right)^3}{\left(1 - \frac{6\rho}{\pi}\right)^3} d\rho, \quad (1.4.4)$$

with the analytical solution

$$\int_{x_1}^{x_2} \frac{1 + (ax) + (ax)^2 - (ax)^3}{(1 - ax)^3 x} dx = \frac{3 - 2ax}{(ax - 1)^2} + \log(x) \Big|_{x=x_1}^{x_2}. \quad (1.4.5)$$

Dropping the lengthy notation for η we end up with

$$\frac{\Delta F}{N} = kT \left(\frac{3 - 2\eta_2}{(\eta_2 - 1)^2} - \frac{3 - 2\eta_1}{(\eta_1 - 1)^2} + \log \left(\frac{\eta_2}{\eta_1} \right) \right). \quad (1.4.6)$$

The analytical solution is compared in fig. 1.4.1 with numerically results which have been calculated before the analytical solution was found. In the following, the free energy difference is identified with the difference in chemical potential $\Delta\mu$ as it is the driving force of the nucleation.

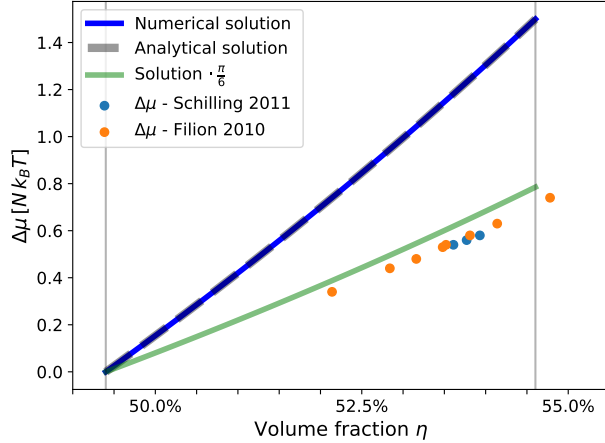


Figure 1.4.1.: Free energy difference per particle between the metastable liquid phase and the coexistence phase. Values by Schilling et al. 2011[9] and Filion et al. 2010[8] deviate from the shown result, but we assume that a factor of $\frac{\pi}{6}$ in the calculations is missing in either this or their calculation, as the modified green curve collapses rather accurately on the literature values when choosing $\eta_{\text{freeze}} = 0.5$.

Coming back to the free energy landscape of eq. 1.4.1, we see that it exhibits a maximum at a radius called $R_{\text{crit.}}$. The interpretation of this radius is, that if a cluster surpasses the critical radius it is likely to keep growing until the system settles at the equilibrium solid fraction. Here, a cluster is defined as a structure having a locally crystalline like ordering. The critical radius, simply calculated by setting the derivative of eq. 1.4.1 to zero, is given by

$$R_{\text{crit.}} = \frac{2\gamma}{\rho\Delta\mu}, \quad (1.4.7)$$

and the height of the barrier at the critical radius is given by

$$\beta\Delta G(R_{\text{crit.}}) = \frac{16\pi\gamma^3}{3\rho^2(\Delta\mu)^2}. \quad (1.4.8)$$

The classical critical radius depending on the volume fraction is depicted in fig. 1.4.2 for a first

impression of the cluster sizes that we are expecting for nucleation. The interfacial surface tension for this often is given by $\gamma \approx 0.6 k_B T \sigma^{-2}$, but its precise value is under debate. Thus, we may stick to one of the recently calculated values of $\gamma = 0.589 k_B T \sigma^{-2}$ by Bültmann and Schilling 2020[17].

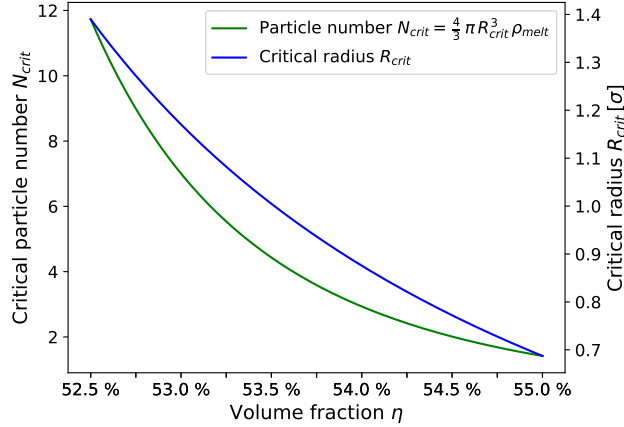


Figure 1.4.2.: Critical radius R_{crit} . calculated from CNT depending on the volume fraction η . The critical radius obtained by our calculation is rather small, but when using the chemical potential calculated by Schilling or Filion[8, 9], the critical cluster size is of the order $N \approx 50$ at intermediate metastable volume fractions, corresponding closer to typical fluctuations of the largest cluster found in simulations.

1.5. Computer precision and chaotic behavior

The finite floating point precision impacts the outcome of the simulation as it constitutes a many body problem with chaotic behavior. In this section it is shown that, for example, even smallest variations of positions lead to radical changes of the simulation after a certain number of steps. It is used to emphasize the importance of rigorously saving the simulation state if it is supposed to be restarted from a file, or with changing measurement intervals. Also, it reminds us that the numerical simulation only is an approximation that never follows the phase space trajectories of the true system.

The exponential growth of induced variations in a chaotic system can be visualized by comparing a reference simulation with a perturbed one. In fig. 1.5.1, the mean of the squared displacements of all particles is recorded between such a pair of simulations. The perturbation consists of a slight push of $10^{-10}\sigma$ to one particle's position, which is comparable to missing some floating point precision during saving and loading.

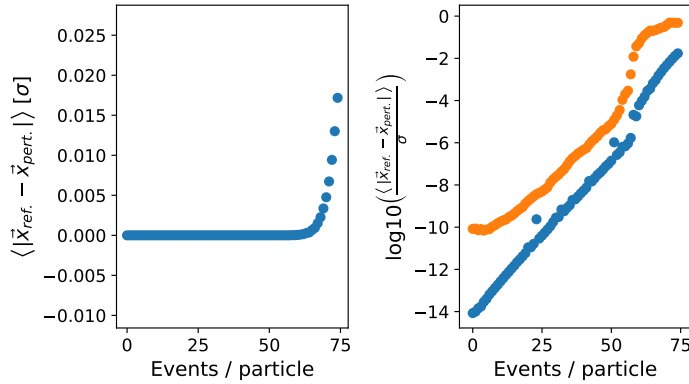


Figure 1.5.1.: Mean difference of particle positions in the reference and perturbed simulation.

The blue lines show the same data, while the orange curve shows the maximum deviation present at each step. For comparison with datasets using the system time δt as units, a rough conversion is given by $T \approx (\#steps) \cdot \frac{1\delta t}{60\text{steps}}$, where a step is defined as one event execution per particle.

The maximum deviation first consists only of the initial perturbation but then increases similar to the mean deviation.

The assumption, that the simulations remain the same to a certain point and then suddenly diverge, can be made when observing only the left side. However, in the logarithmic representation we see that the perturbation actually grows exponentially as long as it is small. It deviates from this exponential growth at the point when reference and perturbed simulation become more or less independent of each other.

The small bumps seemed to be an artifact of the periodic boundary conditions but on a second look this was not validated. What causes these deviations therefore remains hidden.

The challenge this behavior poses is that any perturbation pushes the system to a completely different trajectory. In the context of EDMD simulations, we can examine the case when a measurement of some quantity is performed. For this purpose, all particles have to be propagated to the global time. To not perturb the system with this extra calculations, an exact copy of the particle positions has to be saved prior to the measurement. Following it, this copy is then used to restore the unperturbed system.

Similarly recalculating an event for the FEL at some point of time is not possible as the outcome will vary in the last digits. For this reason, it becomes necessary to save all precalculated events of the simulation in order to be able to restart it from a file.

However, facing this challenge makes it possible, for example, to resimulate an interesting part of a trajectory from some saved checkpoint with a higher measurement frequency to resolve more details.

1.6. Comparison to real world experiments

Starting in 1986 with the experiments by Pusey and Megen[18], hard sphere like systems have been synthesized in the laboratory. Today, a large variety of them is known, but further systems are being developed aiming at controlling stability and sphere size as well as reducing the possible impact of charges on top of the spheres because the Coulomb interaction alters the behavior of the system. Common to all is, that the hard spheres are suspended in some fluid and that usually its mass density has to be matched to the mass density of the hard spheres to prevent sedimentation. An exception to this may be nucleation experiments that have been done in space without gravity. See Doherty et al. 1998[19]. Further, it is necessary for optical measurements to match the refractive index of the fluid and the spheres because otherwise the probe becomes opaque.

The absence of the bath in simple hard sphere simulations constitutes a large difference to those experiments in the laboratory. It has been argued, that this only introduces a difference of the time scale which can be compensated by using the characteristic diffusion time as the unit of time. However, a discussion on the possibility of hydrodynamic effects changing the behavior of the laboratory system compared to simulations is ongoing at the moment. See Radu and Schilling 2014[20] compared to Fiorucci et al. 2020[11].

A more subtle detail is the missing mode spectrum of the suspending fluid within the cavities between the dispersed spheres. However, showing its importance requires further investigation. Nevertheless, simulations probably could approximate the real world more accurate by including the suspending fluid, but the proliferation of particles raises calculation times by orders of magnitude.

A further difference is given by the spatial geometry and extent of the simulation. The geometry in simulations is often chosen with the unphysical setup of periodic boundary conditions (PBC) which are used to avoid surface effects. The impact of this geometry is studied well because the setup is very commonly used.

Concerning the spatial extent, simulations are mostly confined to very small systems in comparison to experimental setups leading to a further major difference between the measurement geometries. While the experimentalists usually probe a large continuous volume of hard spheres in a suspending fluid, the theorists mostly use many disjunct volumes, as each subvolume can be processed by a single CPU, making simple parallelization of the calculations possible.

Measurement techniques, to determine the nucleation state of the experiment, also vary. Light scattering on the growing crystal planes is often used in experiments to measure the crystallinity of a sample because the information of each single particle position is most of the time not ac-

cessible. Subsequently, a nucleation time can be defined by when an overall crystallinity is obtained. In comparison, theorists have access to all positions, but no simple measurement like light scattering available. Instead, they use a variety of cluster finding algorithms to determine crystalline local structures. The nucleation time then can be defined by the mean waiting time until a stable crystalline phase is found, for example, Filion et al. 2010[8].

A discussion on possible definitions of the nucleation time is done in section 3.7. Furthermore, we will discuss the nucleation behavior of the common simulation geometry in section 3.8.1 and the corresponding one for the infinitely large volume in section 3.9.2. Finally, this leads to a possible explanation of the discrepancy between the nucleation rates measured in simulations and laboratory based experiments.

2. Simulation details and testing

During the course of the master thesis, an event driven molecular dynamics (EDMD) simulation code has been developed. The EDMD approach is chosen because the actual dynamics of the system is required to search for possible memory effects. This means, that simulations only probing the phase space of the system, like Monte Carlo (MC) simulation schemes, are not suited.

Furthermore, the discontinuous potential of the hard spheres is an obstacle not easy to face in regular molecular dynamics (MD) schemes in which the Newtonian equations of motion for the particles are numerically integrated. As the EDMD approach even requires these discontinuities, it is very well suited for the purpose at hand.

The key points of the program, possible extensions and a thorough testing are presented in the following, starting with the units of the simulation. They are σ the sphere diameter as the unit of length, m the mass of a particle as the unit of mass, $k_B T$ as the unit of energy and resulting from these $\delta t = \sqrt{m/(k_B t)} \sigma$ as the unit of time. The unit system is also used throughout this thesis.

2.1. Algorithm and simulation details

In this section, we will highlight the main differences to regular MD simulation schemes which are another main tool to probe the dynamics of molecular systems. Furthermore, we will stick to the hard sphere example when discussing the EDMD simulation but it should be kept in mind that the approach allows to simulate all systems governed purely by potentials made of step functions.

The decisive difference between EDMD simulations and regular MD schemes is that, instead of evaluating all pair and external forces on each particle and then evolving the whole system accordingly to the next time step, EDMD simulations do not use a predefined time step. Instead, the system is evolved from one event time to the next one which is defined by the next collision of two particles within the simulation box.

The employed event prediction algorithm follows the approach proposed by Bannerman et al. 2014[21] closely and is discussed in the next section.

2.1.1. Event driven molecular dynamics (EDMD)

For the prediction of events in EDMD simulations an overlap function $f_{ij}(t)$ between particles i and j is defined. It uses the squared quantities because they are easily accessible.

$$f_{ij}(t) := |\vec{r}_j(t) - \vec{r}_i(t)|^2 - \sigma^2 \quad (2.1.1)$$

$$\text{with } \vec{r}_i(t) = \vec{r}_i(t_0) + (t - t_0) \vec{v}_i(t_0), \quad (2.1.2)$$

$$\Delta t := t - t_0,$$

$$\vec{v}_{ij}(t) := \vec{v}_j(t) - \vec{v}_i(t),$$

$$\vec{r}_{ij}(t) := \vec{r}_j(t) - \vec{r}_i(t),$$

$$\Leftrightarrow \vec{r}_{ij}(t) = \vec{r}_{ij}(t_0) + \Delta t \vec{v}_{ij}(t_0)$$

$$f(t) = (\vec{r}_{ij}(t_0) + \Delta t \vec{v}_{ij}(t_0))^2 - \sigma^2 \quad (2.1.3)$$

$$f(t) = |\vec{r}_{ij}(t_0)|^2 + \Delta t^2 |\vec{v}_{ij}(t_0)|^2 - 2\Delta t \vec{r}_{ij}(t_0) \cdot \vec{v}_{ij}(t_0) - \sigma^2 \quad (2.1.4)$$

The overlap function has the property that it is negative for two particles being closer than their diameter, zero at collision and positive if neither overlapping nor touching. The task to calculate the next collision thus is to calculate the roots of eq. 2.1.4.

Solving for Δt with $rr := |\vec{r}_{ij}(t_0)|^2$, $vv := |\vec{v}_{ij}(t_0)|^2$ and $rv := \vec{r}_{ij}(t_0) \cdot \vec{v}_{ij}(t_0)$ has the solution given in eq. 2.1.5.

$$\begin{aligned} 0 &= rr + vv \Delta t^2 - 2rv \Delta t - \sigma^2 \\ \Leftrightarrow 0 &= \Delta t^2 - \frac{2rv}{vv} \Delta t + \frac{rr - \sigma^2}{vv} \\ \Leftrightarrow \Delta t &= -\frac{rv}{vv} \pm \sqrt{\left(\frac{rv}{vv}\right)^2 - \frac{rr - \sigma^2}{vv}} \end{aligned} \quad (2.1.5)$$

A caveat when executing on a floating point machine, however, is present as can be seen when we consider which solution is the relevant one. For a possible collision it is necessary that the two particles move towards each other or mathematically $rv < 0$ as the relative velocity is required to be opposite to the relative position.

Further, the quadratic formula has two solutions, corresponding to the beginning and the ending of the overlap. Due to the entry being prior to the exit, we conclude that we are interested in the smaller solution which is

$$\Delta t = \frac{-rv - \sqrt{(rv)^2 - vv(rr - \sigma^2)}}{vv}. \quad (2.1.6)$$

Now, for the case where the distance of the spheres is already close to the diameter of the spheres, we find $(rv)^2 \gg (rr - \sigma^2)$ which results in a cancellation of two large numbers leaving a small number. Floating point number operations are inherently badly suited at this point, as they tend to large inaccuracy in this case. However, reformulating eq. 2.1.6 by making use of the third binomial formula, leads to the mathematically identical expression

$$\Delta t = \frac{(rr - \sigma^2)}{-rv + \sqrt{(rv)^2 - vv(rr - \sigma^2)}}. \quad (2.1.7)$$

Comparably, eq. 2.1.7 does not contain a cancellation of the type seen before and hence is better suited for the use in the computer simulation, as stated by Goldberg 1991[22].

The event prediction algorithm, which was proposed by Bannerman et al. 2014[21], works by differentiating 4 cases:

1. If $rv > 0$, the particles move away from each other leading to a collision time of $\Delta t = \infty$
2. If $rr < \sigma^2$, an overlap is present resulting in an immediate collision time of $\Delta t = 0$
3. If $(rv)^2 - vv(rr - \sigma^2) \leq 0$, the two particles miss each other, including touching without momentum transfer, resulting in a collision time of $\Delta t = \infty$
4. If none of the before is true, the particles collide and Δt is calculated by eq. 2.1.7

All possible collision times for a particle are then stored in a queue that is sorted by the event times and is called particle event list (PEL). From the PEL the first entry is then passed to the global future event list (FEL). This procedure initially takes place for all particles to set up the system and later on only for those particles involved in the execution of an event.

While this is the simplest description, in section 2.1.2 the implementation of some widely used measures to reduce redundant calculations and the use of a cell system to reach $\mathcal{O}(N)$ computation time are further discussed.

An important detail to take care of is the possibility of scheduled events which have become invalid due to an earlier collision of one of the particles. This is handled by assigning an interaction count to each particle that is stored at precalculation time with the event. When the event is drawn from the FEL and the interaction count of one of the particles has increased in the meantime, the event is said to be invalidated. Depending on which particle had an event in the meantime the invalidation either causes no action or a recalculation of new events.

2.1.2. Details concerning the implementation

As the simulation code is based on an earlier Monte Carlo code for hard spheres a complete walk through the whole program would be extensive. Hence, we will focus on key points to understand the details of the simulation program. Furthermore, differences to the MC program are mentioned for the readers that are familiar with it.

The *Event* struct

We start with the basic *Event* struct which includes 6 entries that are shown in tab. 2.1.1. The

Datatype	Name of entry
(double)	time
(int)	event_type
(Particle*)	particle
(void*)	partner
(int)	particle_count
(int)	partner_count

Table 2.1.1.: Content of the *Event* struct.

time variable holds the time for when the event is scheduled in the future. The *event_type* variable is either set to 0 or 1 and indicates if the event is a cell transfer or a collision of two particles respectively. To include hard walls or other elements further types of events can be defined.

The *particle* variable is a pointer to the particle for which the event has been precalculated, while the *partner* variable is defined as a void pointer. This allows, to either interpret it as a particle pointer for the collision type event or as an integer pointer to the index in the current cells' neighbors list for transfer events.

In the last two rows the interaction counts for particle and partner are listed as well. As the destination cell in a transfer event does not require an interaction count, the *partner_count* variable is only used for collision events.

The *event* struct is used for all events throughout the simulation. For read and write operations with the HDF5 file format, the struct *event_data* is available which uses only integer indexes, instead of pointers.

The *Particle* class

The *Particle* class is comparable to the one from the MC code basis. Its MC related attributes have been removed and additional key variables and concepts will be discussed in the following.

First, a vector for storing events, called *backupEvents*, has been added to make it possible to keep events from the precalculation for the case of the first event being invalidated. The idea of reusing events is discussed in many publications, for example, Bannerman et al. 2011[23] states that the memory cost increases linearly with more backup events while the speedup does not increase much for more than two stored events. It also has been argued by Donev et al. 2005[24] that the added complexity can not account for the increase in efficiency.

However, in our own simulations a calculation time reduction of more than 10% was observed and the cost of complexity and memory was seen as moderate. The difference might be explained by the fact that the systems under consideration in this thesis have a rather large particle density which leads to more invalid collisions.

In the context of reusing precalculated results, it should also be mentioned that after a cell transfer the recalculation of events can be reduced to possible partner particles of only the new neighboring cells, leading to only 1/3 of the calculation time in this case. But, as the systems under consideration are very dense, transfer events often constitute less than 5% of all executed events. Thus, the increase in efficiency is assumed to be too costly on the complexity side and not implemented. For sparse systems, however, it might make sense to include an *updatePEL()* routine as transfers are more frequent.

Further key differences to the former MC particle type are the variables *total_interactions* and *particle_delayed_time*. The first is the variable for book keeping of interactions. The second is necessary because the particles are not synchronized in time. Nevertheless, the behavior is well defined by the ballistic equation of motion. To actually take the whole configuration to one point of time, the *transferToTime()* function of the particle is provided. This is obviously necessary for measurements, including snapshots.

To take the whole configuration to one point of time, the *transferToTime()* function of the particle is provided. This is obviously necessary for measurements including snapshots.

As mentioned before, the system behaves chaotically even under slightest changes like a rounding error from an extra floating point operation. Therefore, measuring at different rates during a simulation changes it, as we have observed in section 1.5, that the system may keep close to the undisturbed trajectory only for about 50-100 events/particle. The program employs copies of the configuration because it is of desire to measure quantities and take snapshots without disturbing the simulation. This is costly in terms of memory but makes simulation resets or higher sampling rates at interesting points possible within a well defined trajectory.

In detail, the measurement without perturbing the system is implemented by making a backup

copy of the working configuration just before a measurement is taken. The working trajectory then is disturbed by the measurement and afterwards replaced with its state before the measurement from the backup configuration.

A second copy is carried throughout the simulation including the full simulation state to save and reset it at any point during the simulation without writing to the file. This could be useful to do a committer analysis in which a cluster at different stages is sampled multiple times with different perturbations but may include other uses as well.

The *Box* class

The box of the simulation remained in principle the same as in the previous MC code. A new element is the *neighbors_lookup* table which contains the indices to the elements in the cells' array *neighbors*, where pointers to the cells that share a surface are stored. It is used to identify which cell a particle has to be transferred to during a cell transfer event.

Furthermore the *Update()* routine now takes care of all quantities depending on the length of the box, and the *rescale()* routine is a simple rescaling of the edge lengths with an additional *Update()* call.

The *Scheduler* class

While the aforementioned elements of the program are also required for the EDMD simulation, the *Scheduler* class certainly contains the most distinct parts of the program. It keeps track of all events to come, predicts new events and orchestrates the execution of the events. The essential functions are discussed in the following subsections while some basic properties are shortly highlighted here.

First of all the *Scheduler* holds the future event list (FEL) in which at least one event per particle is stored. As discussed within section 2.1.2, the simulation is capable of saving the complete state of a trajectory, including all precalculated events. For this purpose, the *reset_FEL_array* is available. Furthermore, the *Scheduler* includes the *global_time* variable that holds the latest event execution time.

We may also note the importance to preallocate all arrays that are used in the event calculations for the efficiency because the collision prediction routine is executed about 30 times per step and particle, and easily accounts to a few billion function calls during a small simulation.

Scheduler::predictTransfer()

As the name suggests, this function predicts the next cell transfer of a particle due to its movement. It calculates the position of the particle at global time which, for a valid state of the simulation, always lies within its cell. Denoting for each dimension i , the position of a particle within its cell by r_i , its velocity by v_i , and the cell's length by l_i , we can formulate for each dimension the equations

$$t_{i1} = -\frac{r_i}{v_i} \quad \text{and} \quad t_{i2} = \frac{l_i - r_i}{v_i} \quad (2.1.8)$$

which describe the times $t_{i1/2}$ when the particle pierces the cell's left and right boundaries in dimension i . A negative time corresponds in this case to a boundary crossing in the past. A time comparable to 0 means that the particle is on the edge of its cell and a positive time means that the boundary crossing is in the future. By going through the different possible cases for t_1 and t_2 , we find the resulting next crossing time for each case as shown in tab. 2.1.2.

t_1	t_2	Result	Case
>	>	invalid	-
>	=	$t_{\text{crossing}} = t_1$	0
>	<	$t_{\text{crossing}} = t_1$	1
=	>	$t_{\text{crossing}} = t_2$	2
=	=	invalid	-
=	<	$t_{\text{crossing}} = t_1$	3
<	>	$t_{\text{crossing}} = t_2$	4
<	=	$t_{\text{crossing}} = t_2$	5
<	<	invalid	-

Table 2.1.2.: Possible results for left and right crossing time with resulting choice of next crossing time. $>$, $=$ and $<$ are to be read as for example $t_1 > 0$. The case indicates the case number within the simulation code.

By collecting the next crossing times for each dimension and taking the minimum of these times the exit time of the particle from its cell is determined.

The return value of the routine is an *Event* where the partner is a pointer to the corresponding entry in the box' *neighbors_lookup* table. The index is between zero and five corresponding to the six possible neighbor cells sharing a surface with the current cell of the particle. Each valid case represents a distinct neighbor cell and its index within the cell's *neighbors* array is clearly defined by the cell setup routines. The indices within the neighbors array are matched with the defined cases is tab. 2.1.3.

dimension	boundary	case	index
x	front	0	12
	back	1	13
y	front	2	10
	back	3	15
z	front	4	4
	back	5	21

Table 2.1.3.: Overview of the cells' *neighbors* indices directly sharing a surface for 3 dimensions. As the indices hardly follow any simple pattern they are explicitly noted at this point. Obviously the cell consists of a front and a back boundary in each dimension. The corresponding case numbers are identical to the ones from tab. 2.1.2.

Scheduler::predictCollision()

The prediction of collision times has already been discussed in section 2.1.1. The implementation in the program first calculates all necessary scalar products, while accounting for the periodic boundary conditions, and in a second step returns the collision time depending on the case at hand. The here presented algorithm is only valid for single sized particles but it can be extended to polydisperse systems as is shown in section 2.5.1.

As this routine is executed throughout the simulation multiple times, it has been tried to optimize its efficiency as far as possible. For example, calculating only necessary results for the next case differentiation has been tried but without significant increase in efficiency and for better readability the prior version has been used instead. In either case, if more efficient calculations are found, it is useful to implement them at this point.

Scheduler::setupFEL()

This routine fills the FEL of the simulation. For this purpose it iterates through all particles and calls *setupPEL()* for each of them. The PEL in turn is set up by predicting the next cell transfer as well as the next collisions with all particles within the 3^d cells in d dimensions directly surrounding the particle. From all predicted events only such with finite times are then written to the *backupEvents* vector that is the PEL of the particle.

For the FEL only the top event of each particle's PEL is then used. Because other events from the PEL might move on to the FEL at later times the top event that was pushed to the FEL has to be erased from the PEL.

Scheduler::executeTransfer()

The execution of a transfer event is accomplished by the particle's *MoveBetweenCells()* routine. The departure cell is taken as the event particle's own cell, while the information about the

destination cell is contained in the event's *partner* variable. It points to the address within the lookup table of the box where the index of the pointer to the destination cell, in the departure cell's neighbors array, is deposited.

Scheduler::executeCollision()

The velocity change after a collision between particles i and j of same mass, with corresponding velocities $\vec{v}_{i/j}$ and relative position $\vec{r}_{ij} = \vec{r}_j - \vec{r}_i$ is given by

$$\vec{v}'_i = \vec{v}_i + \left(\frac{rv}{rr} \right) \vec{r}_{ij}, \quad (2.1.9)$$

where the definitions from eq. 2.1.5 of the scalar products, rr and rv , for the relative positions and velocities are used. An own derivation, also for arbitrary masses, is given in section A, as most textbooks only show the momentum transfer in the center of mass frame.

Scheduler::executeEvent()

The execution of an event works in multiple steps. At first the topmost *Event* is copied from the FEL where it is deleted. Next the validity of the interaction counts of the particle (*cond1*) and its partner (*cond2*) are evaluated. The validation is nothing more than a comparison of the interaction count when the event was scheduled with the present interaction count. The conditions are stored in boolean variables, as they are used in the following flow statements. Furthermore, the validation of the partner is not necessary in the case of a transfer event but for better readability performed either way.

It follows a distinction between 5 cases which are given by:

Valid transfer (*event_type==0* and *cond1*)

The transfer is executed, the global time is evolved to the event time, the particle's PEL is rebuilt and its next event pushed to the FEL.

Valid collision (*event_type==1* and *cond1* and *cond2*)

The collision is executed, the global time is evolved to the event time, for both participating particles new PEL's are built and each top event is pushed to the FEL.

Invalid transfer (*event_type==0* and not *cond1*)

The particle must have had an interaction previously where a new event was scheduled for it, thus no action is taken.

Invalid collision due to particle (*event_type==1* and not *cond1*)

The particle must have had an interaction previously where a new event was scheduled for it, thus no action is taken.

Invalid collision due to partner (*event_type==1 and not cond2*)

Only the partner had an interaction previously where a new event was scheduled for it, thus a new event for the particle is required. As the particle had no further interactions, the events in the backup are still valid and the first entry is pushed into the FEL. In case the *backupEvents* array is empty, the PEL is rebuilt and its first entry pushed to the FEL instead.

The order of the cases might be exchanged except for the last two. This is, because the last one indirectly assumes *cond1* to be true which is guaranteed by the case before.

Furthermore, the routine counts the occurrence of each case, to monitor numbers of collisions, transfers and invalidated cases by type. This is not required by the simulation but can be helpful for understanding the system and simulation.

2.1.3. The simulation periphery

For the simulation to work, some more surrounding is required. This is briefly discussed in the following.

Inout and ch5md

As suggested by the names, the former comprises the read and write routines of the simulation while the latter one holds routines dealing with the h5md format.

Setup

The setup routines are called mainly at the beginning of a simulation to either set up a simulation from a file or to completely start a new simulation. So far only the *FCC_init()* routine is written. It initially places all particles on a fcc lattice and assigns the amplitude of their starting velocities by the equipartition theorem to $|\vec{v}| = \sqrt{3} \frac{\sigma}{\delta t}$. The directions are chosen randomly under the constraint to keep the center of mass at rest.

Tools

This is the toolbox of the simulation holding routines to measure quantities like mean squared displacement, radial distribution functions and the cluster finding routine. Functions only used within the simulation like an overlap or minimal distance routine for the compression are included at this point as well.

The cluster finding algorithm will be highlighted at this point, as the details of it are necessary to compare the direct data of cluster sizes with the data of other groups.

It is based on the q6q6-bond-order parameters first described by Steinhardt et al.[25]. The local structure around a particle i with N_b neighbors is characterized by the quantity

$$\bar{q}_{lm}(i) = \frac{1}{N_b} \sum_{j=1}^{N_b(i)} Y_{lm}(\hat{r}_{ij}) \quad (2.1.10)$$

in which $Y_{lm}(\hat{r}_{ij})$ are the spherical harmonics evaluated in the direction of the relative position of particles i and j in a given coordinate system.

$\bar{q}_{6m}(i)$ suffices to indicate the local fcc structure of hard-sphere crystals. Based on $\bar{q}_{6m}(i)$ a normalized vector $\vec{q}_6(i)$ is defined with elements for $m = -6$ to $m = 6$ given by

$$q_{6m}(i) = \frac{\bar{q}_{6m}(i)}{\sqrt{\sum_{m'=-6}^6 |\bar{q}_{6m'}(i)|}}. \quad (2.1.11)$$

As a minimum threshold for the scalar product $\vec{q}_6(i) \cdot \vec{q}_6(j)$, we choose 0.6 to identify a pair of particles i and j as “orientational bonded”. To define a solid particle we set the minimum number of bonded neighbours to be $n_B > 8$, similar to ten Wolde et al.[26] or Schilling et al.[9].

2.2. Testing of the simulation code

To verify the dynamics of the simulation, we measure the long time self-diffusion constant and the radial distribution function of the stable hard sphere liquid, as there are measurements and theoretical predictions in the literature to compare with.

2.2.1. Diffusive behavior

The diffusive behavior of particles in a liquid can commonly be separated in three distinct regimes. First, the short time diffusion which can be understood as the random movement of the particles in their momentary cage within the fluid. Second, a subdiffusive phase in which the particles are repelled for the first time by their nearest neighbors. And third, the long time diffusion to describe the random propagation of the particles through the fluid over time. As the ballistic hard sphere system enters into the long time diffusion almost at once, due to the lack of the suspending fluid, only this is measured.

We use unwrapped coordinates to reduce finite size effects. In this case, the long time movement of a particle is governed by the relation eq. 2.2.1, which was first described by Einstein 1905[27].

$$D_L^S = \lim_{t \rightarrow \infty} \frac{\langle (\vec{r}(t) - \vec{r}(0))^2 \rangle}{2 d t} \quad (2.2.1)$$

In the equation, D_L^S is the long time self-diffusion constant which will in the following be denoted only by D_L , $\vec{r}(t)$ is the position of a particle at time t , d is the number of spatial dimensions and $\langle \dots \rangle$ is the expectation value of the ensemble.

For the measurement, a reference position of all particles at one point of time and the set of unwrapped positions is used. The mean squared distance between the two estimates the ensemble average. Subsequently, we use the linear regression of $\langle x^2 \rangle(t)$ to find the diffusion constant D_L .

The simulated testing systems are characterized in tab. 2.2.1. The equilibration is done at the final volume fractions, up to $\eta = 50\%$, while above this an initial volume fraction of $\eta_i = 45\%$ is used to obtain a fluid rather than a solid during the equilibration phase. As some measurements are within the metastable regime, we check that no clusters are present in the box during the measurement as they would reduce the averaged diffusion.

Parameter	Value
N	16384
eq. events/particle	5000
pr. events/particle	20000
η_i	5% ... 50 %
η_f	5% ... 54 %

Table 2.2.1.: Input parameters of diffusion test systems.

The resulting diffusion constants depending on the volume fractions are shown in fig. 2.2.1 alongside with values from the literature for the same hard sphere fluid.

As it can be seen, the EDMD simulation is capable of reproducing the diffusion constant for the hard sphere liquid. Consequently, we expect the dynamics of it to accurately approximate the purely ballistic hard sphere system.

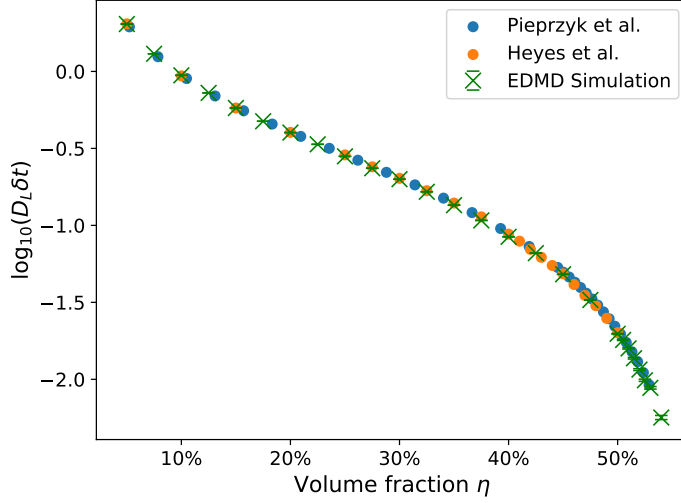


Figure 2.2.1.: Logarithmic plot of long time diffusion constant for the hard sphere liquid as measured in our own simulations as well as measurements from Pieprzyk et al. 2019[28] and Heyes et al. 2007[29].

2.2.2. Radial distribution function

A further well known quantity for the hard sphere system is the radial distribution function. It can be described by the theoretical Percus-Yevick approximation, which is used for comparison. In fig. 2.2.2, an overview for a range of volume fractions is shown from the same data sets used in section 2.2.1. As expected, no particles come closer than the diameter of a sphere which verifies that no collisions are missed. Furthermore, the liquid shells become more visible for higher volume fractions. At very high volume fractions, we also find a new peak at $r < 2\sigma$ which indicates the local structuring on the path to nucleation. By comparison to the Percus-Yevick approximation, the radial distribution functions for two volume fractions are shown with the corresponding theoretical solution in fig. 2.2.3.

As highlighted by Hansen and McDonald 2006[30], the theoretical approximation has some flaws as can be seen by observing, that $g(r)|_{r=1\sigma}$ is too low in the Percus-Yevick approximation. However, the two radial distribution functions align closely which shows that the developed simulation code is capable of producing accurate data in other contexts as well.

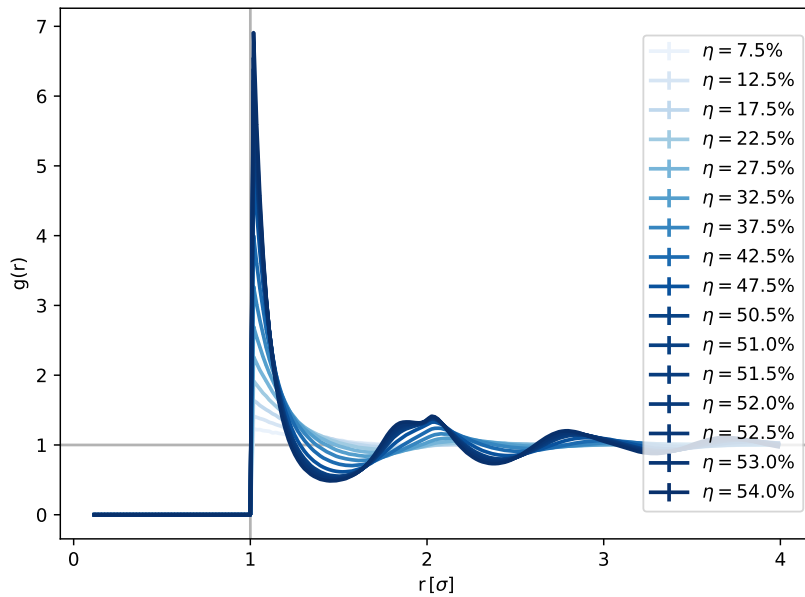


Figure 2.2.2.: Radial distribution functions for a range of volume fractions, with color lightness corresponding to the volume fraction of the liquid.

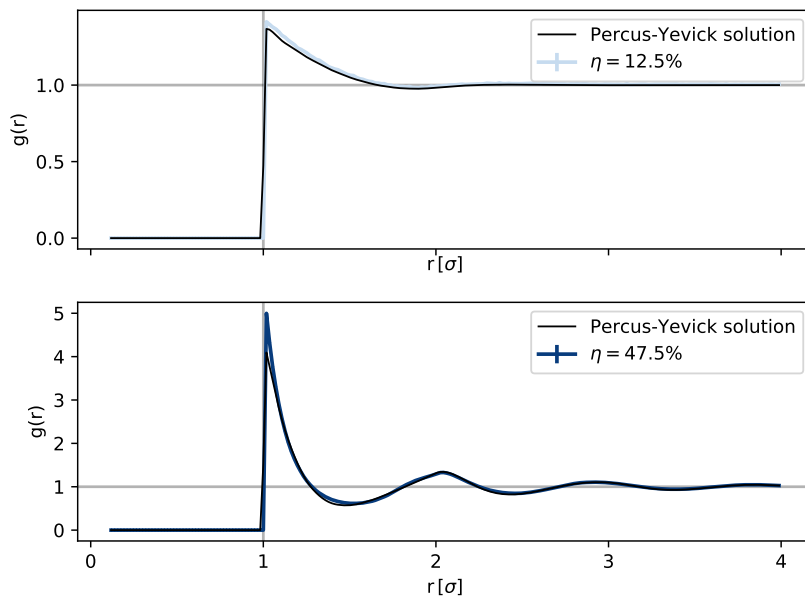


Figure 2.2.3.: Radial distribution function of the particles in the hard sphere liquid at a low and at a high volume fraction illustrated along the theoretical Percus-Yevick approximation.

2.3. Estimate of required resources

To choose system parameters in a reasonable manner, calculation times and file sizes of the simulation have been characterized. This was necessary as the program was supposed to run on the NEMO high performance computing cluster where hard boundaries are set on calculation times. Therefore, trespassing can cause tremendous loss of data if not correctly caught by the program.

2.3.1. Calculation time estimate

The calculation time of the program was tested for a large range of different system sizes up to almost 9 million particles in the fluid state. As can be seen in fig. 2.3.1, the calculation time increases proportional to the system size for the execution of a step as well as for a measurement in the fluid state. The calculation cost being of $\mathcal{O}(N)$ enables the study of large systems. Furthermore, the execution time of a single event and the measurement time are given by the slopes. As discussed on the example of fig. 2.3.2 the dependence of the measurement routines on the largest cluster size were not seen here as possible clusters remained rather small during these simulation times.

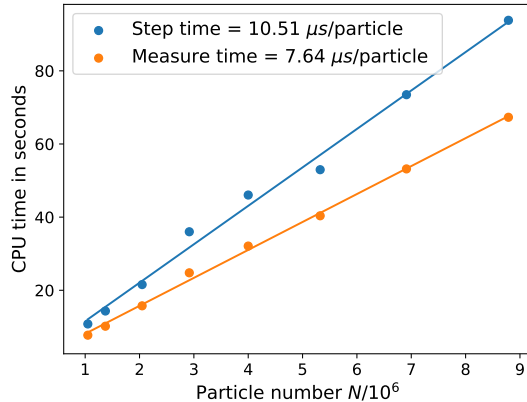


Figure 2.3.1.: Overview of CPU time required for calculating a simulation step, consisting of an event for each particle, as well as a measurement of relevant quantities of the system. As assumed for a simulation algorithm with a theoretical $\mathcal{O}(N)$ calculation effort, the data points can be well described by a line. As the CPU time is clearly related to the further workload of the CPU during the calculation it is also expected to find fluctuations if the other workload of the machine is not strictly controlled.

The effect of larger clusters was only investigated after extraordinary long runtimes were traced back to these. The q6q6-order parameter routine was tested for larger clusters in a nucleating simulation with about 1 million particles within the box. As can be seen in fig. 2.3.2, the

calculation cost of the cluster finding routine can be described with a quadratic dependence on the largest cluster. To give an impression of what this means, we can use the calculation costs of a simulation step from fig. 2.3.1 being about $t_{\text{step}} \approx 10 \mu\text{s}/\text{particle}$. Therefore, the execution of one step takes about 10 s for 1 million particles. If a measurement is performed every 10th step, the calculation cost of the measurements without a large cluster remains below 10%. But as the largest cluster grows to a few hundred thousand particles in size, the measurements can make up 30% and more of the calculation cost, or for a fixed number of steps, increase the calculation time by about 50%. This previously unseen effect lead to actual data loss as the combination of NEMO's policy and EDMD simulation program did not result in a save shutdown of the program after breaching the wall time limit of four days.

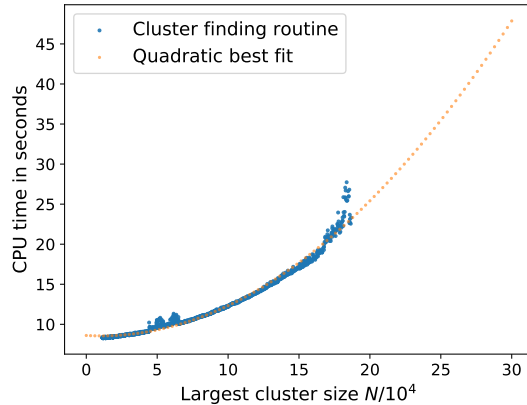


Figure 2.3.2.: Calculation time of the q6q6 order parameter cluster finding routine with an increasing largest cluster size during one nucleation. The quadratic best fit indicates that the calculation effort can be approximated by $\mathcal{O}(N_{\text{lc}}^2)$, with N_{lc} being the size of the largest cluster.

2.3.2. File sizes estimate

A further important constraint for the simulations are the produced amount of data. To get an impression of the file sizes, the required memory for configuration snapshots, reset steps and other measurements were measured prior to the actual simulations. The results of a single snapshot and a single simulation checkpoint are shown in fig. 2.3.3. While the former only contains all positions and velocities the latter contains all positions, velocities, the FEL, all PEL's, delayed times, the cell's first particles and properties of the box. It can be seen that the file size is proportional to the system size as each particle adds a pair of positions, velocities etc. to the saved data.

The memory costs of other measurements have been left out of fig. 2.3.3, as these can only amount to substantial file sizes if measurements at each step for long simulations are done.

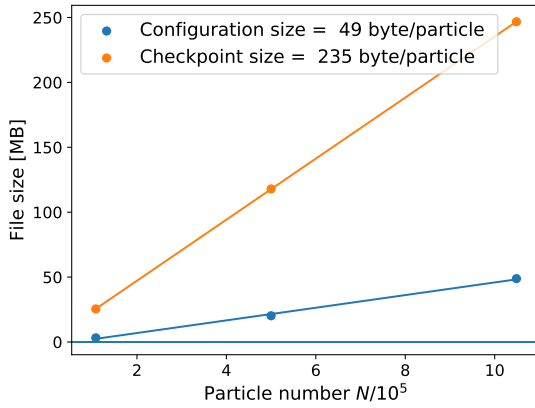


Figure 2.3.3.: File sizes of a configuration snapshot and a full simulation state at different system sizes with their linear regressions. While for three data points the procedure is not statistically meaningful, it still remains a useful tool to extract the slope that corresponds to the required memory per particle for a configuration snapshot or a simulation checkpoint.

2.4. Preliminary data for equilibration test

The motivation to develop the simulation code is based on the interest in nucleation rates of the hard sphere system at varying volume fractions. To observe a nucleation, the volume fraction of hard spheres has to be changed rapidly from lower ones where the system is in the stable fluid phase to higher ones where the stable fluid phase becomes metastable. If this state is evolved in time, nucleations can be observed as stochastically distributed events. To measure those without artifacts originating from the simulation procedures, some parameters were tested within reasonable ranges prior to the data production.

Mainly the number of equilibration steps as well as the initial density before the volume quench are tested because both may impact the local ordering directly after the quench. Thus, we performed some smaller data series to evaluate if and when these effects might come into play. The used test system is characterized by the parameters given in tab. 2.4.1.

The general behavior of the fluid is analyzed by inspecting the cluster size distribution over time. Its average over all trajectories is shown in fig. 2.4.1 together with the same data smoothed by a Gaussian filter matrix. The smoothing is employed afterwards, as otherwise only fluctuations are visible at low count rates.

From fig. 2.4.1 we can see the reaction of the fluid after the quench into the metastable state. As there are rarely any clusters present in the stable liquid and the spatial configuration of the particles requires some time to rearrange into the local ordering, no clusters are found directly

Parameter	Value
N	16384
eq. events/particle	100 ... 20000
pr. events/particle	200000
η_i	5% ... 49 %
η_f	54 %

Table 2.4.1.: Input parameters of test systems probing the dependence on equilibration steps and initial density.

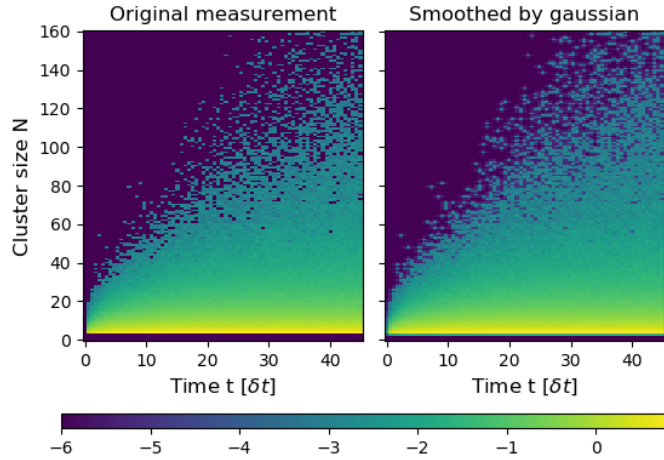


Figure 2.4.1.: Heat map of the mean cluster distribution over time. The diagram encompasses 800 trajectories of 16384 particles each. The coloring indicates the decadic logarithm of the average cluster occurrence in a box which corresponds to a free energy in the stationary case.

after the quench. In the later evolution we then see how clusters form, and soon after begin to nucleate leaving the y-axis range of the diagram.

To identify differences between the ensembles with varying start parameters, the quantity defined in eq. 2.4.1 is used. To circumvent complications due to zero values, they are fixed to values below the regular signal. Three samples of this comparison are shown in fig. 2.4.2 and fig. 2.4.3 for different lengths of equilibration phase and different initial densities. The coloring indicates the value of $\Delta_{p(N,t)}$ defined by

$$\Delta_{p(N,t)} = \log \left(\left| \frac{p_i(N,t)}{\langle p(N,t) \rangle} - 1 \right| \right) . \quad (2.4.1)$$

As mentioned before, the quantities $p_i(N,t)$ and $\langle p(N,t) \rangle$ are smoothed by a Gaussian filter because the number of included samples is with 100 trajectories per series not sufficient to

produce smooth distributions at the given sampling rate. Thus, without smoothing mostly fluctuations are visible.

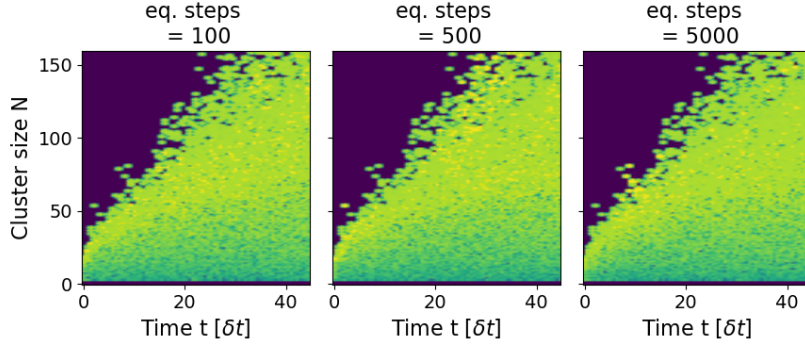


Figure 2.4.2.: Heat map of differences between the cluster distributions within simulations carried out with varying lengths of the equilibration phase. The quantity used for coloring is defined in eq. 2.4.1. Yellow indicates a large difference, whereas blue indicates a small difference. Providing a legend of the coloring is omitted as $\Delta_{p(N,t)}$ has no further use than to indicate differences and actual values do not add any use.

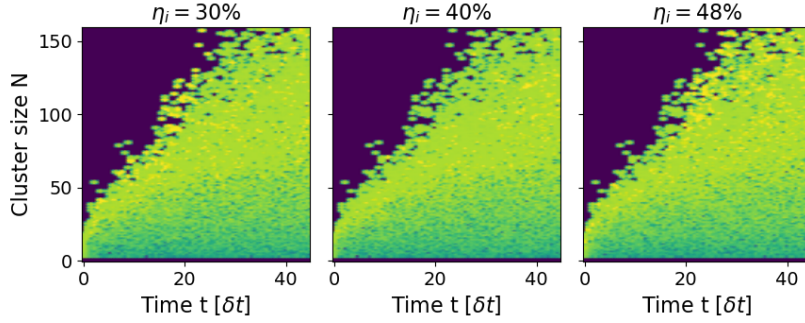


Figure 2.4.3.: Heat map of differences between the cluster distributions within simulations carried out with varying the volume fraction of the liquid during the equilibration phase. The quantity used for coloring is defined in eq. 2.4.1. Yellow indicates a large difference while blue indicates a small difference. Providing a legend of the coloring is omitted as $\Delta_{p(N,t)}$ has no further use as to indicate differences and actual values do not add any use.

On first sight, none of them differ in their general behavior. The blue region in the top left corner indicates no difference between the simulations directly after the quench because no clusters were present in the stable liquid and also no clusters have formed yet. The features visible on the edge between the zero region and the nonzero region on the other side are the same, because they are features of the mean distribution shining through. Actual differences that are not due

to fluctuations would only be visible within the green and yellow nonzero region, but no such difference is observed.

While it seems like the set for an initial volume fraction of $\eta = 0.4$ and eq. steps = 5000 includes a little less irregular fluctuations, strong differences remain absent. Especially interesting is the ensemble with eq. steps = 100 because here the length of the equilibration phase is similar to the time the initial perfect crystal configuration takes to melt. For this reason, one could expect that a significant part of these configurations might directly crystallize again but instead we do not find any significant impact.

A more quantitative analysis is given by calculating the mean nucleation rates for each set of trajectories. The maximum likelihood estimator that is used for this purpose as well as its uncertainty is discussed in section 3.8.2. The results for the different data sets are depicted in fig. 2.4.4.

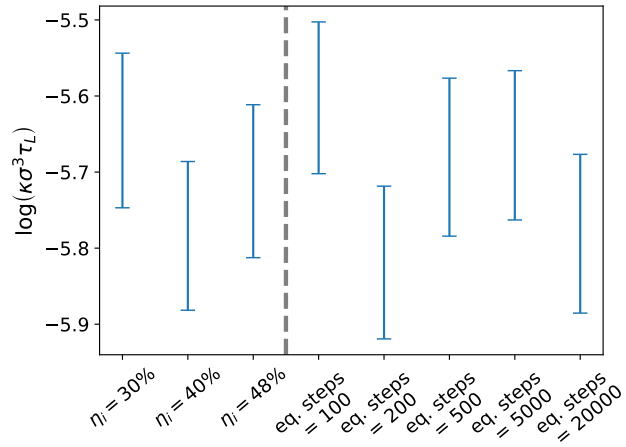


Figure 2.4.4.: Comparison of nucleation rates under CNT assumptions for different initial densities during equilibration with eq. steps fixed at 5000, as well as varying eq. steps with η_i fixed at 45%.

As we can see, no significant difference can be observed between the nucleation rates even for the extreme short equilibration phase of 100 events per particle. For this bold setting the rate is a little higher but still in accordance with the other measurements within its statistical uncertainty.

Overall, we can conclude in this chapter that as long as parameters are set within broad but reasonable boundaries no systematic influence is expected.

2.5. Extensions for future studies

The program at this state is capable of simulating large systems including compression and relaxation. While it has been used to study the nucleation of the monodisperse hard sphere fluid in this thesis, additional features have been developed to suit the code for further studies. Polydispersity in the sense of radius and mass distributions have been implemented and roughly tested, as well as individual cluster tracking, to enable a detailed study of spatial information regarding the clusters. The state of these two features and their use are described in the following two sections.

2.5.1. Polydispersity for varying radius and mass

Polydispersity has been included in the simulation to make it more comparable to actual experiments in which monodisperse spheres are practically not achieved. Also, the phase diagram becomes richer as the complexity of the system increases as is shown for example by Pusey et al. 2009[31].

Within the implementation, especially the prediction of collisions has to be adjusted. When looking at the derivation of eq. 2.1.7 it is found that σ being the former diameter of a sphere in the monodisperse case only has to be changed to $\sigma = R_i + R_j$. In eq. 2.5.1 and eq. 2.5.2 the same definitions of scalar products are used as before in section 2.1.1 where the monodisperse case is discussed.

$$\Delta t = \frac{(rr - (R_i + R_j)^2)}{-rv + \sqrt{(rv)^2 - vv(rr - (R_i + R_j)^2)}} \quad (2.5.1)$$

Then, in a physical model with particles that are constituted by some matter with constant density the change of radius is also accompanied by a change of the mass. This has to be taken into account when assigning the velocities after a collision as shown in eq. 2.5.2.

$$\begin{aligned} \vec{v}_i' &= \vec{v}_i + \frac{2m_j(rv)}{(m_i + m_j)(R_i + R_j)^2} \cdot \vec{r}_{ij} \\ \vec{v}_j' &= \vec{v}_j + \frac{2m_i(rv)}{(m_i + m_j)(R_i + R_j)^2} \cdot \vec{r}_{ij} \end{aligned} \quad (2.5.2)$$

A small caveat is given by the fact that the system with different masses requires a new routine to fix its center of mass frame. If this is not considered, unnecessary transition events have to be calculated.

2.5.2. Single cluster tracking algorithm

Following trajectories of single metastable clusters within the fluid can be used to measure their mean lifetimes. Also, the nucleation time can be observed with higher precision as the precursor can be tracked back to only a few particles.

To track individual clusters, they have to be identified in each measurement step because they form out of the liquid and are not numbered and easily distinguishable as the particles are. For this purpose, we can either employ the clusters' participating particles or their center of mass positions. The latter one is used as it is easier to compare and to access in our case because a routine to calculate the center of mass of a cluster already is implemented. Furthermore, less data has to be written and compared. An algorithm based on maximum movement from one time step to the other is tested and yields reasonable results as can be seen in fig. 2.5.1.

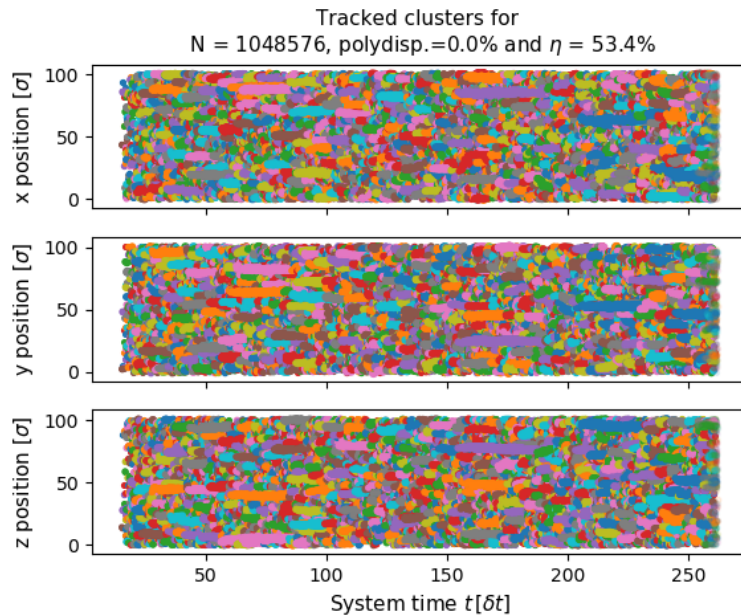


Figure 2.5.1.: Example results of the cluster tracking algorithm in a monodisperse simulation. The three plots are the projections of the box onto the three spatial dimensions over time. Each cluster is given a color to identify it. With it we can see for example that two clusters mingling in one projection are actually some distance apart from each other in an other dimension.

In this example only small metastable clusters that dissolve after some time are present but also nucleation events can be visualized in this kind of plot. They are easily identified as the width of the line is proportional to the diameter of a sphere with a volume corresponding to the clusters volume under the assumption of it being spherically symmetric.

Information about the lifetime and size of the fluctuations derived from the analyzed example trajectory shown in fig. 2.5.1 are depicted in fig. 2.5.2.

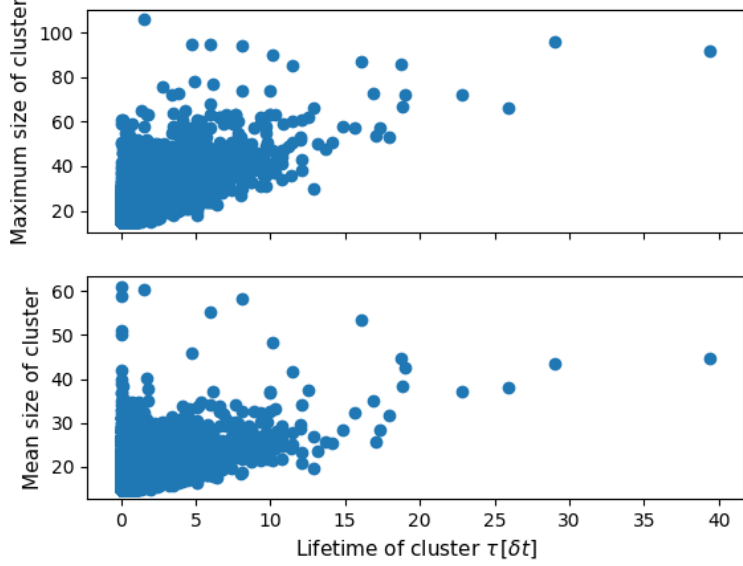


Figure 2.5.2.: Example of lifetime depending on maximum (top) or mean (bottom) size of the metastable cluster. The size is defined by the number of particles in the cluster.

First we note that both the maximum size and the mean size can be used to measure the scale of the fluctuations as the results mostly vary by the scaling. Further, we can extract from the diagram that at a volume fraction of $\eta = 53.4\%$ there are a lot of small to medium and few large sized clusters. The small ones show short lifetimes up to about $10\delta t$, while some large ones show lifetimes of more than $15\delta t$. The large fluctuations with short lifetimes might be caused by merging and splitting of clusters because the simple algorithm does not test for such. The overall impression is that the fluctuation distribution is compact with a small but very far reaching tail towards the large lifetimes as well as towards the large cluster sizes.

3. Data Analysis

3.1. Parameter choice of the simulated system

As an integral part of this work large scale simulations have been executed on the NEMO High performance computation (HPC) cluster. The input parameters of the simulated systems are given in tab. 3.1.1.

Parameter	Value
N	1048576
eq. events/particle	1000
pr. events/particle	20000 ... 60000
η_i	45.0 %
η_f	53.1% ... 53.4 %

Table 3.1.1.: Input parameters of large scale simulations on the NEMO HPC cluster. The varying steps during production are a result of the fact that 20000 steps were estimated to be calculated within 3 days leaving 1 day of buffer to the hard wall time limit of 4 days. Due to the increasing calculation cost of the q6q6 cluster routines for large clusters, the wall time limit was still breached. Without proper reset steps the datasets could not be restarted without large calculation overhead because all lost data would need to be replaced. Moreover, the broken reset steps within the files would have to be removed prior to further simulations. Therefore, the last proper version of the files was used resulting in varying simulation lengths. Nevertheless, only very few simulations had an early breakdown without a nucleation event.

The simulations comprise four series at volume fractions of $\eta = 0.531, 0.532, 0.533$ and 0.534 where each series consists of 500 trajectories. Therefore, a total number of about half a billion particles have been simulated in the metastable fluid at each volume fraction.

The volume fractions have been chosen to probe nucleation rates to the lowest possible limit. As nucleations have been observed down to volume fractions of $\eta = 53.2\%$, the lowest volume fraction was set to just below this value because it was expected to still find enough nucleation events to measure their rate with the large number of trajectories.

The size of the systems was chosen comparably large with about 1 million particles. These large systems intuitively seem to be in conflict with the long induction times. However, by using CNT

as a guideline it can be shown that the computational effort for simulating nucleation events does not increase significantly with increasing system size. As the calculation time per unit of simulation time is proportional to N , it is at a given volume fraction also proportional to the volume V :

$$\frac{T_{\text{CPU}}}{\delta t_{\text{Sim.}}} \propto N \propto V \quad (3.1.1)$$

Further we expect the nucleation time in terms of the system time $\langle \tau_{\text{Nucleation}} \rangle$ to be proportional to the inverse of the system volume if assuming a nucleation rate density independent of time:

$$\langle \tau_{\text{Nucleation}} \rangle \propto \frac{1}{V} \quad (3.1.2)$$

As the required CPU time for a nucleation event is simply proportional to the product of $\langle \tau_{\text{Nucleation}} \rangle$ and the calculation time per unit of system time we can conclude:

$$\langle T_{\text{CPU}} \rangle \propto \frac{T_{\text{CPU}}}{\delta t_{\text{Sim.}}} \cdot \langle \tau_{\text{Nucleation}} \rangle \propto \frac{V}{V} = \text{const.} \quad (3.1.3)$$

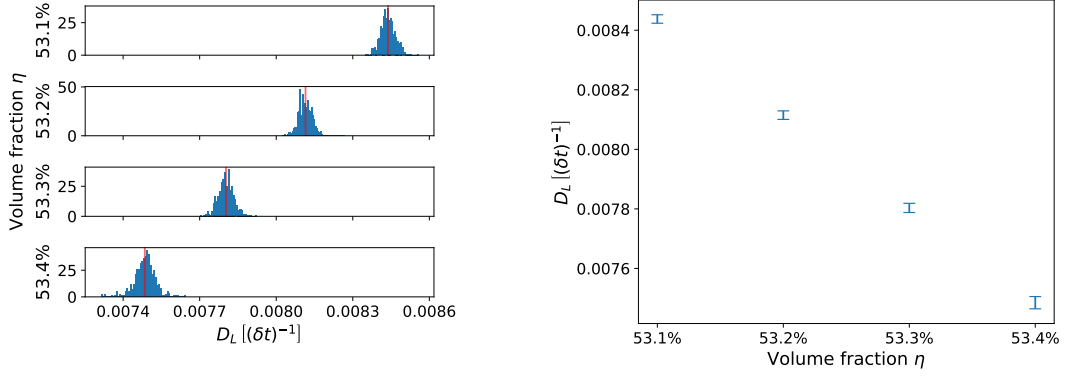
Thus, the size of the system is only relevant to be chosen smaller if ordering processes are important for the system, as the initial induction time would be independent of the system size. This might be the case for polydisperse systems, but in the monodisperse case the above reasoning was found to hold true.

Another objective that has to be considered is that less configuration snapshots of the system can be stored, as they require a lot of memory space. If one is interested in quantities like $g(r)$ this is not a problem, as the necessary statistics can be either derived from a large set of small snapshots or from a small set of large snapshots. The task, however, to resolve and store the dynamics of a configuration of a growing cluster would require using smaller system sizes, as files easily grow to many GB's in size.

3.2. Long time diffusion time scale

As introduced in section 2.2.1, the long time self-diffusion is measured. The results fluctuate only little as can be seen in fig. 3.2.1, where the diffusion constants from the linear regressions to the MSD trajectories are depicted.

The diffusion coefficients are used to make the time scales of different experiments comparable. It is based on the idea that the fundamental mechanisms for nucleation and cluster growth do not vary between different hard sphere like systems, but are only scaled by the varying diffusion times. Furthermore, there are theoretical predictions for the relationship of short time and



(a) Histograms of the slopes for the linear regressions to the mean squared displacements. The histograms are for $\eta = 0.531, 0.532, 0.533, 0.534$.

(b) Mean of the histograms with the uncertainty on the mean given by $\sigma_{\langle D_L \rangle} = \sigma_{D_L} / \sqrt{n}$ with n being the number of measurements included in the average.

Figure 3.2.1.: Comparison of long time self-diffusion constants at different volume fractions as histograms and means with uncertainty.

long time diffusion. Thus, it is possible to compare experiments where the short time diffusion behavior is better accessible with the ballistic simulations in which only the long time diffusion constant is measurable.

As it can be seen in fig. 3.2.1, the diffusion constants can be measured with a relative standard deviation of $\sigma_{D_L}/D_L \approx 1\%$. Hence, it does not introduce large uncertainties when normalizing time related quantities by the diffusion time $\tau_{D_L} = D_L^{-1}$.

3.3. Cluster size distribution over time

The cluster size distribution of the system can be used to test the assumption of Markovian dynamics by trying to find a Fokker-Planck equation describing the time evolution of the distribution. This has been done for the Lennard-Jones system by Kuhnbold et al. 2019[2]. Testing the trajectories shown in fig. 3.3.1 and fig. 3.3.2 in a similar fashion is a promising comparison, but due to time constraints of this thesis it is not attempted. We can still illustrate some characteristics of the metastable fluid directly after and long after the quench, as it compactly shows some main features of the systems behavior.

The cluster size distributions are the averages over all trajectories at a given volume fraction. While they are normalized by the number of included measurements, they have not been normalized by the volume. The maximum cluster size is set to 160, as above this value only nucleating

trajectories can be seen. Also, a logarithm to the base of 10 is used and absent cluster sizes at a given time step have been fixed to a value below the minimal signal, as the logarithm requires nonzero values.

The logarithm is used because the distribution then can be interpreted as a quantity proportional to a free energy. This is justified, for one, by assuming that the cluster size distribution represents the corresponding probability distribution and, secondly, that stationary states may fluctuate in a free energy landscape where the probability for a particular state with some energy ΔE is given by a Boltzmann distribution $p \propto \exp\left(-\frac{\Delta E}{k_B T}\right)$ from which follows that $\log(p) \propto \Delta E$.

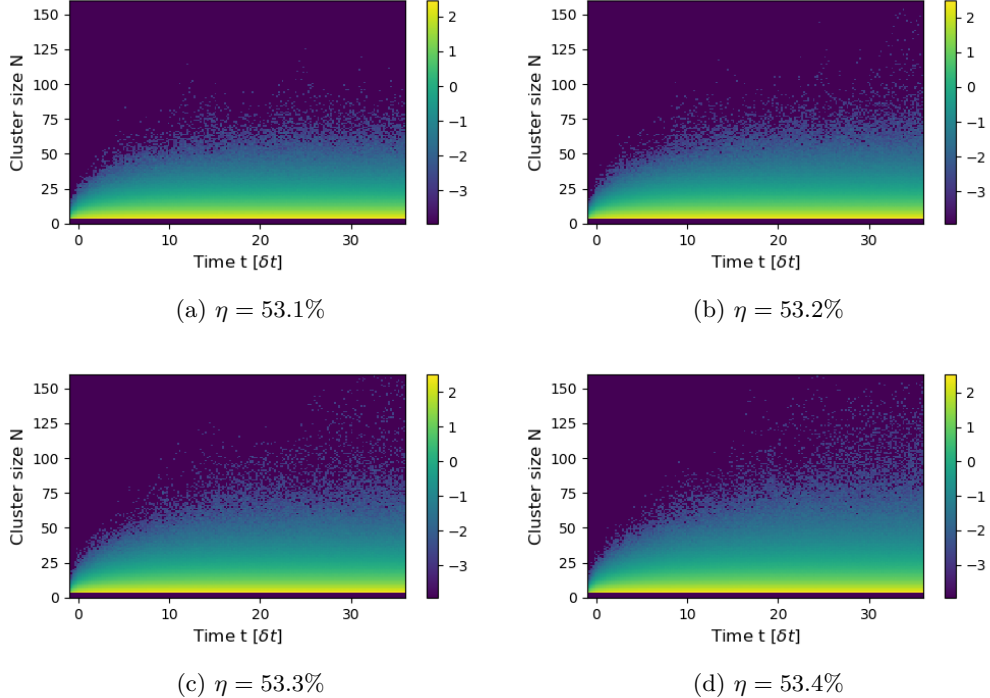


Figure 3.3.1.: Decadic logarithm of cluster size distributions for different volume fractions in the initial phase after the quench. Clearly visible is the initial ordering process after which the distribution becomes mostly stable.

In fig. 3.3.1, we can see the initial phase after the quench. As the fluid before the quench was at a volume fraction of $\eta = 45\%$ only very little local ordering is present directly after the quench. Depending on the volume fraction, this changes within the first $15\delta t - 25\delta t$ after which the distribution becomes stable. One possible explanation for the different duration is that more particles are required to find their ordering, as the clusters tend to be larger for higher volume fractions.

To compare the system time with the more intuitive number of collisions per particle, we can use that at the given volume fraction we find $1\delta t \approx \frac{60\text{events}}{\text{particle}}$. When further using a collision probability of about 40% for each executed event, we find that $1\delta t \approx \frac{25\text{collisions}}{\text{particle}}$. As a result we can conclude that it takes a few hundred collisions for each particle to build up the local ordering.

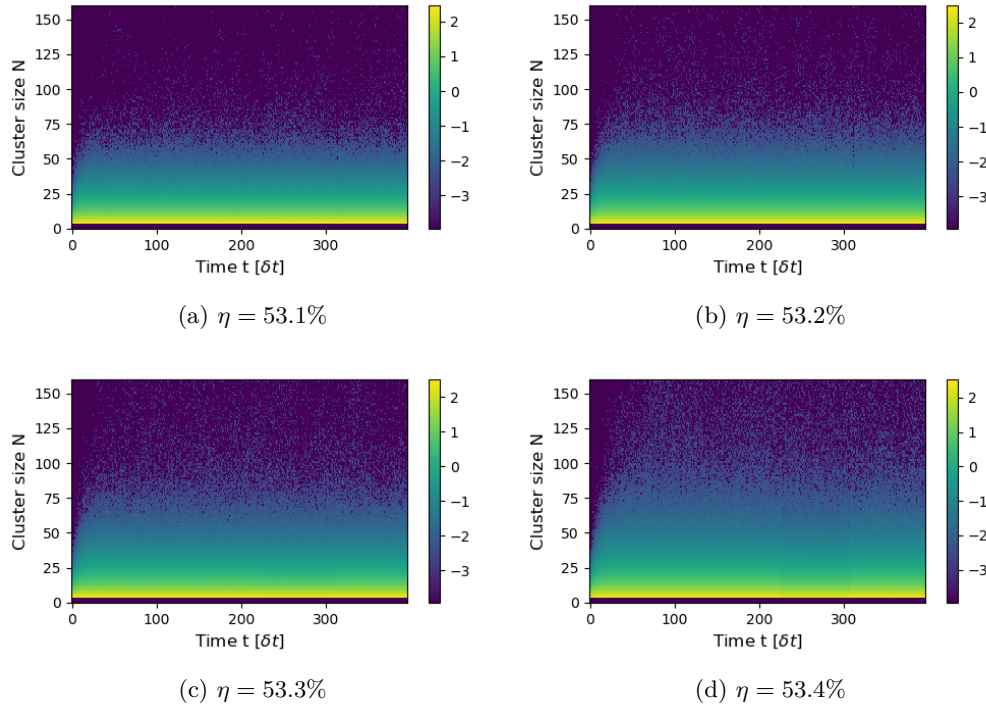


Figure 3.3.2.: Decadic logarithm of cluster size distributions for different volume fractions during the waiting time. While the initial ordering process is only visible on the very left, the distribution in the metastable fluid is found to be mostly constant over prolonged periods of time. Only rare nucleation events leave the size range of the diagram.

The diagrams in fig. 3.3.2 show a zoomed out version of the same data depicted already in fig. 3.3.1. We see that the distribution that is reached at the end of the initial phase remains stable over prolonged periods of time. Only the nucleation events, which account for most of the probability at largest cluster sizes, indicate that this is not a stable process but only a metastable one. Nevertheless, this does not mean that it simply can be approximated as a stationary process because when considering the ensemble as a whole, at any point of time, phase transitions take place at various parts of the system.

3.4. Autocovariance functions of largest cluster in the metastable fluid

The autocovariance function (ACF) of the largest cluster contains information about how long a single cluster persists as the largest cluster within the volume. This is because fluctuations of clusters at different points of the volume are expected to be independent of each other and only the size of a distinct cluster should be correlated in time.

The autocovariance function is defined by eq. 3.4.1. There, $N_{lc}(t)$ is the number of particles in the largest cluster at time t , $\langle N_{lc} \rangle_t$ is the corresponding average over time and thus $X(t)$ describes the deviations from the average. The autocovariance function furthermore is normalized by $\langle X^2 \rangle$, the variance of the data, such that $ACF(0) = 1$.

$$ACF(\tau) = \frac{\langle X(\tau) \cdot X(0) \rangle}{\langle X^2 \rangle} \quad (3.4.1)$$

$$\text{with } X(t) = N_{lc}(t) - \langle N_{lc} \rangle_t \quad (3.4.2)$$

The ACF is calculated from the largest cluster measurement for each trajectory. But only those parts of the measurements that did not involve strong cluster growth are used because after a nucleation event the largest cluster size surely is correlated in time. Therefore, the ACF's in fig. 3.4.1 show the temporal correlations of the largest cluster in the metastable fluid.

The decay of the autocovariance functions indicates that structural fluctuations persist for longer times at higher volume fractions. From the coloring, that corresponds to the maximum cluster size within the trajectory, we can conclude that the fluctuations tend to be larger at higher volume fractions. Moreover, for $\eta = 53.4\%$ a signal from nucleation events might not be completely negligible anymore. Overall, the larger metastable clusters were also seen before in the cluster size distributions in section 3.3.

The time scale on which the ACF decays corresponds closely to the initial ordering time observed for the cluster distribution directly after the quench. Furthermore, it also corresponds to the lifetimes of large clusters found in the single example of the individual cluster tracking algorithm (fig. 2.5.2). This leads to the conclusion that these three observations all show the same time scale of local ordering processes within the metastable fluid.

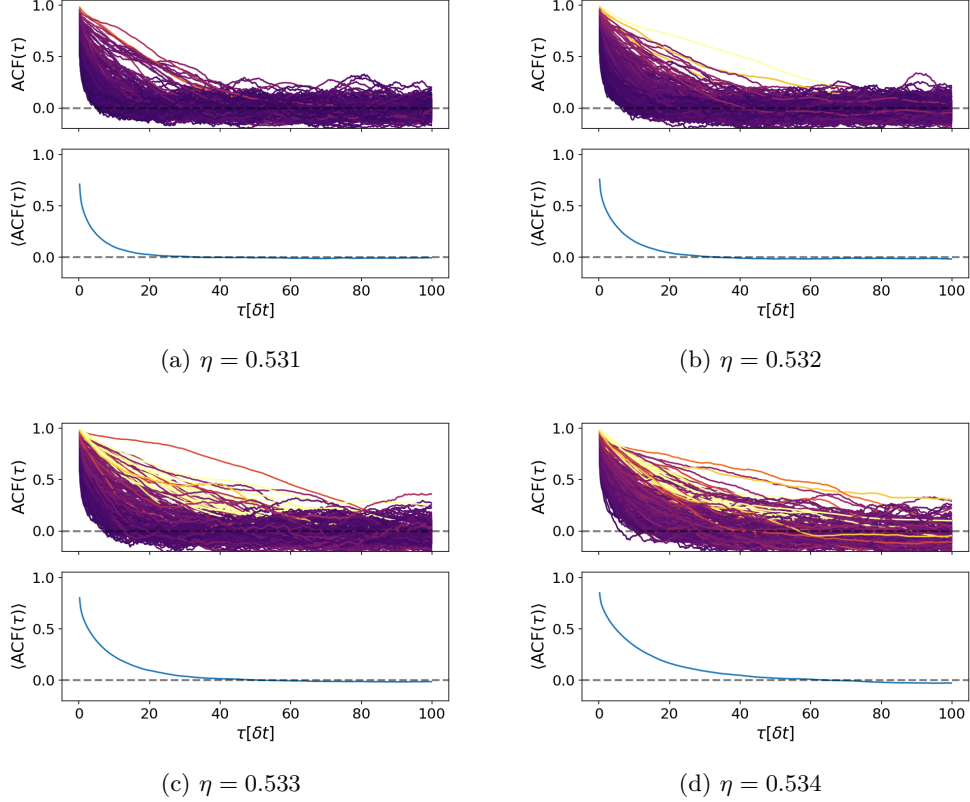


Figure 3.4.1.: Comparison of autocovariance functions in the metastable fluid. The top of each diagram depicts all trajectories with coloring for the largest cluster size within the used time interval. The lightest color thereby indicates a largest cluster of more than 500 hundred particles which is a nucleation event. As they are rare in the given selection, the data represents the metastable fluid well. The bottom of each diagram shows the average of the above one with decay times of $15\delta t - 35\delta t$ depending on the volume fraction.

3.5. Cluster growth and constant attachment rate

Once the clusters reach a certain size, they are expected to grow with new particles being attached to the surface at a constant rate. This leads to a growth with a proportionality of $N \propto t^3$ as shown in eq. 3.5.1, with k being the constant attachment rate, N the number of particles in a specific cluster, A the surface of the cluster, R the radius of the cluster and ρ_{solid} the bulk density which for large clusters is a good approximation of the cluster density.

$$\dot{N} = Ak$$

$$\left| \begin{array}{l}
 \text{with } N = \frac{4}{3}\pi R^3 \rho_{\text{solid}} \\
 \Leftrightarrow R = \left(\frac{3N}{4\pi\rho_{\text{solid}}} \right)^{\frac{1}{3}}, \\
 \text{and } A = 4\pi R^2 \\
 \Leftrightarrow A = \left(\frac{4\pi 3^2}{\rho_{\text{solid}}^2} \right)^{\frac{1}{3}} N^{\frac{2}{3}}, \\
 \frac{dN}{dt} = \left(\frac{4\pi 3^2}{\rho_{\text{solid}}^2} \right)^{\frac{1}{3}} N^{\frac{2}{3}} k
 \end{array} \right. \quad \begin{array}{l}
 \text{From the bottom left side} \\
 \Rightarrow dN N^{-\frac{2}{3}} = \left(\frac{4\pi 3^2}{\rho_{\text{solid}}^2} \right)^{\frac{1}{3}} k dt \\
 \quad | \quad \text{setting } N(t=0) = 0 \\
 \Leftrightarrow 3N^{\frac{1}{3}} = \left(\frac{4\pi 3^2}{\rho_{\text{solid}}^2} \right)^{\frac{1}{3}} kt \\
 \Leftrightarrow N^{\frac{1}{3}} = \left(\frac{4\pi}{3\rho_{\text{solid}}^2} \right)^{\frac{1}{3}} kt
 \end{array} \quad (3.5.1)$$

As the systems are able to accommodate clusters up to a few hundred thousand particles and mostly just one cluster forms during a simulation, the attachment rate can be measured by a linear regression to the third root of the number of particles in the largest cluster over time. As an example this is visualized for the trajectories at $\eta = 53.2\%$ in fig. 3.5.1.

Subsequently, the slopes of the linear regressions have been collected in histograms shown in fig. 3.5.2. According to eq. 3.5.1, these slopes correspond to constant attachment rates with a prefactor depending on the density within the cluster but as the densities of concern are very close to each other they only introduce a relative difference of 0.5% between the rates of lowest and highest volume fractions. For this reason, the dependence is neglected in the qualitative comparison and the constant attachment rate with its prefactor is defined as $c := k \left(\frac{4\pi}{3\rho_{\text{solid}}^2} \right)^{\frac{1}{3}}$. With this approximation, the equation for the number of particles in a cluster over time, given in eq. 3.5.1, simplifies to the one given before in eq. 3.9.1.

We see from the histograms in fig. 3.5.2, that the distribution is rather spread out but not significantly depending on the volume fraction. An smaller growth rate is only found for $\eta = 53.1\%$. One possible explanation for this behavior could be that the growth by heterogeneous crystallization on the cluster surface leads to a higher growth rate for higher volume fractions as it is less likely for the lower volume fractions. Due to the low statistics at the lowest volume fraction, it is also possible that only a statistical fluctuation is observed.

To investigate if the attachment is diffusion or reaction controlled, we may note that the diffusion constants vary from $D = 0.0081|_{\eta=53.2\%}$ to $D = 0.0075|_{\eta=53.4\%}$. They span a difference of about 7.5% but as the relative statistical uncertainty of the growth rates is of the order of 5% it would require a larger number of samples to find a significant result.

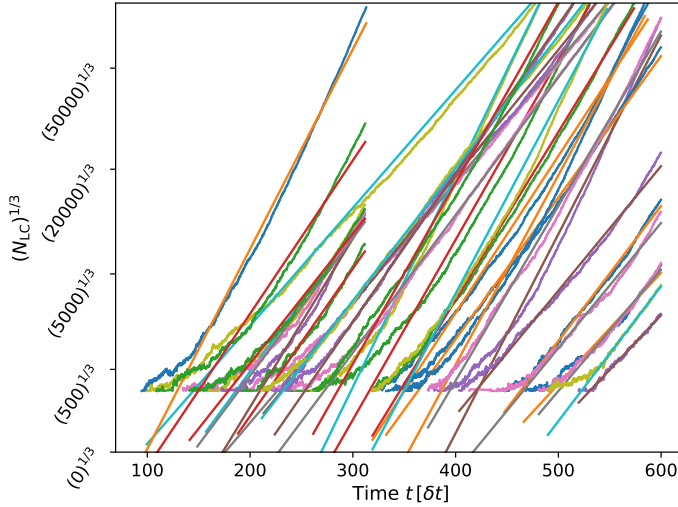
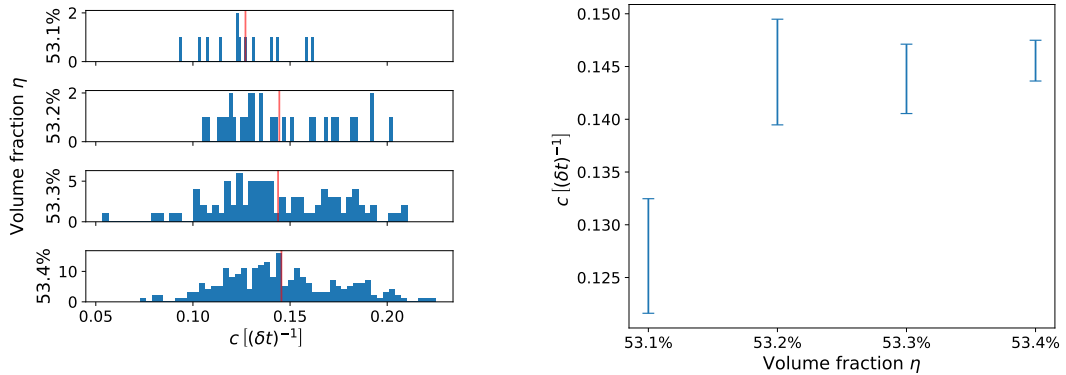


Figure 3.5.1.: Trajectories of the third root of the number of particles within the largest cluster, $(N_{LC})^{1/3}$, over time. The linear proportionality of the data sets is clearly visible and thus, linear regressions are shown along with the data. The cut of some data sets at $t \approx 300\delta t$ is due to the trespassing of the maximum wall time of the NEMO computational cluster. Systems that hosted a nucleation event in the first simulation interval before $T \approx 300\delta t$, contain a too large cluster in the next simulation interval leading to the breach of the wall time limit due to the quadratic effort required for the q6q6 cluster finding routine. It can be assumed that clusters forming just before $t \approx 300\delta t$ might not have been recognized due to this flaw. But the number of trajectories concerned by this is small and the impact is not easy to recognize when looking at the induction time distributions in fig. 3.7.1.



(a) Histograms of the slopes from the linear regressions to third root of the largest cluster during the stable growth process. The histograms are for $\eta = 53.1\%, 53.2\%, 53.3\%, 53.4\%$.

(b) Mean of the histograms with the uncertainty on the mean given by $\sigma_{\langle c \rangle} = \sigma_c / \sqrt{n}$ with n being the number of measurements included in the average.

Figure 3.5.2.: Comparison of growth rates in the constant attachment regime.

3.6. Evaluation of shape descriptors

The tensor of gyration is a very useful tool as it describes the second moments of the position distributions. Thus, it comprises information about the spatial extent in all three dimensions with commonly defined quantities being the radius of gyration, asphericity and anisotropy. See Theodorou and Suter 1985[32].

The tensor of gyration for a structure of N particles with positions $\vec{r}^{(i)}$ is defined by

$$S_{mn} = \frac{1}{N} \sum_{i=1}^N r_m^{(i)} r_n^{(i)} \quad (3.6.1)$$

$$\text{with } \sum_{i=1}^N \vec{r}^{(i)} = 0. \quad (3.6.2)$$

As described by eq. 3.6.2, the matrix S_{mn} is calculated in the center of mass frame for particles with the same mass. The tensor of gyration can be diagonalized with the three eigenvalues λ_1^2 , λ_2^2 and λ_3^2 that are chosen with $\lambda_1^2 \leq \lambda_2^2 \leq \lambda_3^2$. These three eigenvalues correspond to the spatial extents of the cluster within the Cartesian system in which the tensor of gyration becomes diagonal. The aforementioned shape descriptors are defined in eq. 3.6.3 - 3.6.6.

$$\text{(squared) Radius of gyration: } R_G^2 = \sum_{i=1}^3 \lambda_i^2 \quad (3.6.3)$$

$$\text{Asphericity: } b = \lambda_3^2 - \frac{1}{2}(\lambda_1^2 + \lambda_2^2) \quad (3.6.4)$$

$$\text{Acylindricity: } c = \lambda_2^2 - \lambda_1^2 \quad (3.6.5)$$

$$\text{Relative shape anisotropy: } \kappa^2 = \frac{b^2 + \frac{3}{4}c^2}{R_G^4} = \frac{3}{2} \frac{\sum_{i=1}^3 \lambda_i^4}{\left(\sum_{i=j}^3 \lambda_j^2\right)^2} - \frac{1}{2} \quad (3.6.6)$$

For a better understanding of the shape descriptors their meanings are discussed in the following.

Radius of gyration R_G

An averaged radius of the structure. For a sphere with radius R it is given by $R_G = \sqrt{\frac{3}{5}}R$.

Asphericity b

The difference of the largest extent and the average of the two smaller extents. For a sphere, they are the same and the asphericity becomes zero, even though this is also the case for a cube.

Acylindricity c

The difference of the two smaller extents because for a long cylinder they are the same and the acylindricity becomes zero.

Relative shape anisotropy κ^2

A weighted squared sum of the asphericity and the acylindricity that is normalized by the fourth power of the radius of gyration to obtain a dimensionless quantity between 0 and 1. For a sphere, it is zero while it becomes one in the case of all particles being aligned in a straight line.

To spot possible correlations between a cluster's shape and its growth, the radius of gyration, the asphericity and the relative shape anisotropy have been plotted in fig. 3.6.1 depending on the cluster size and further, colored by three scalar quantities characterizing the growth process of each trajectory.

The first of them is the induction time, as early nucleations might arise from less ordered clusters resulting in a higher asphericity. The second is the constant attachment rate during cluster growth in which, accordingly, one may expect that clusters with more defects grow slower and are also less spherical. The third quantity is an exponential initial growth rate which is used to characterize how swift the precursor grows into the later crystal. Again, with the intuition that clusters with a higher asphericity may tend to a slower initial growth as they might be less ordered. For quantifying the initial growth rate, an exponential function has been fitted to the data up to a cluster size of 500 particles.

The representation depending on the cluster size is used to make the different trajectories comparable, as we expect similar behavior for similar cluster sizes. As the cluster size depending on time is almost monotonic for cluster sizes above a few hundred particles, it roughly corresponds to a transformation of the time axis, while the order is only little influenced. Nevertheless, it should be kept in mind that this does not constitute a function anymore.

Finally, the number of particles, as well as the shape descriptors, can span many orders of magnitude making logarithmic scales useful.

For the nucleated trajectories at $\eta = 53.4\%$, an overview produced by this procedure is given in fig. 3.6.1. It includes the three shape descriptors in the vertical direction and the three scalar coloring schemes in the horizontal direction.

From the overview, we get no obvious sign that there are any correlations between cluster shape and growth rates or between cluster shape and the induction time, so no further analysis is performed. Instead we conclude that by this superficial analysis we cannot relate the shape descriptors to the cluster growth. A similar approach for the three scalar quantities that describe the growth process has been done, but neither showing significant correlations.

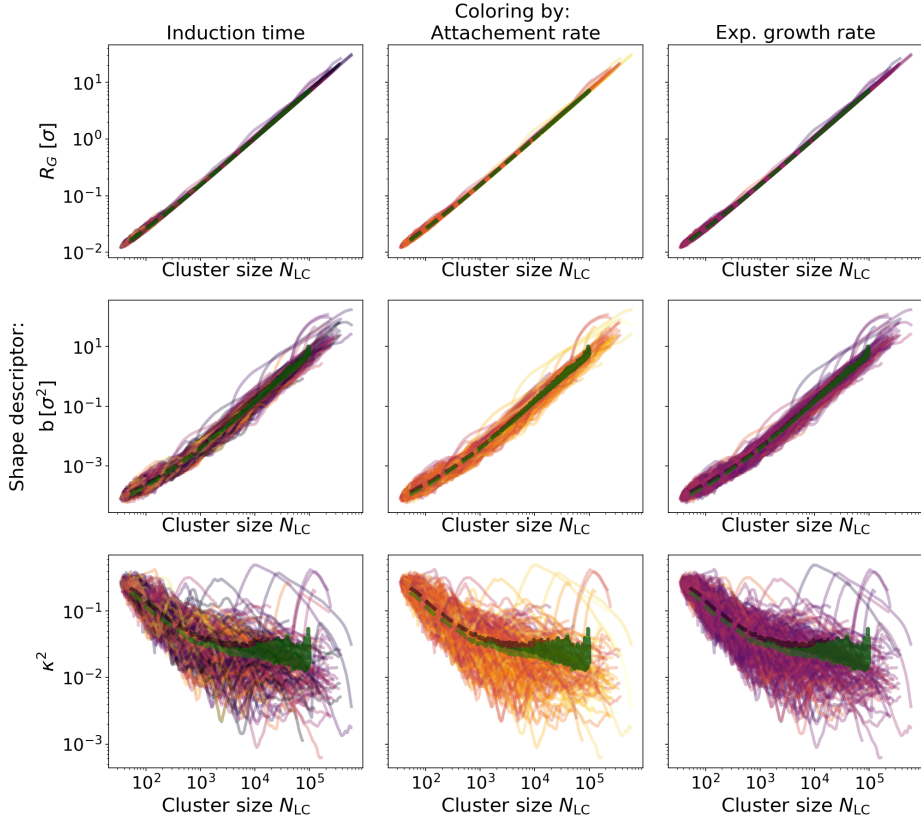


Figure 3.6.1.: Overview of the shape descriptors radius of gyration (R_G), asphericity (b) and anisotropy (κ^2), depending on the size of the cluster are shown. The colors indicate the scalar quantities induction time, constant attachment rate and initial growth rate. Possible correlations are expected to show as color gradients. Further, a smoothed arithmetic mean and median are included in black and green respectively.

Nevertheless, from the calculated means, especially for the anisotropy κ^2 , we can see that up to a size of about 1000 particles the clusters become more spherical while at higher particle numbers this tendency towards a sphere comes to a halt. This could be explained, for example, by the fact that the clusters always exhibit crystal faces leading to some unavoidable asphericity. Another explanation could be that the attachment rate for one crystal face might be higher than for another, as this also would lead to non-spherical growth. As the clusters are rather close to a sphere, however, the attachment rate would also not vary much between the different crystal faces. It also has been observed that very large single crystals of a few hundred thousand particles may only form at volume fractions of $\eta = 53.2\%$. At higher volume fractions, domains form as it seems that heterogeneous nucleation takes place close to the surface of the cluster, leading to new plane orientations that are included into the crystal.

3.7. The nucleation time dilemma

To calculate induction times or average nucleation times, we will require a definition of when a crystal is called nucleated. This means we have to define the point at which a cluster is not merely an unstable fluctuation in the liquid anymore but instead becomes a stable crystalline solid.

Many definitions can and have been used for this purpose. For example, a cluster can be defined to be crystalline as soon as it surpasses the CNT's critical size or a multiple of it. One can also use a committer analysis to find the size where a crystallite keeps growing with a 50:50 chance. The method to rewind a trajectory with a stable crystal back to the point where the cluster's size vanishes is also often applied. A further approach is to fit the growth during later times and extrapolate it to the time when the cluster vanishes.

All these definitions differ only by a delay Δ_τ which is a distribution holding the information of how long it takes for varying clusters to pass from the first criterion to the next.

For example, we can take as a first point the time when a cluster, known to crystallize at later times, is not distinguishable from any other structural fluctuation in the liquid i.e., when the size of the cluster is below some threshold defined by the size of clusters which are regularly present in a given volume.

The second point we can set by either the critical size of CNT or by some other criterion when we are sure that the cluster has stabilized and will only continue to grow.

At the first of these two points, the fluctuation leading to the crystallization occurs but it would be impossible to tell if this precursor is yet to melt or to grow, while at the second point, the crystal is stable. For this reason, the first might be called a precursor nucleation and the second crystal nucleation. Between these two points, we find the time difference to be the time it takes for the precursors to form a stable crystal. This includes also that some precursors might loiter for awhile before forming the stable phase while others pass this gap rather directly.

When calculating a mean induction time, the delay Δ_τ propagates also to the final result and as it is a stochastic distribution its higher moments are also propagated leading to a smaller precision. This means that the induction time depends directly on the definition of crystallization and they are only roughly comparable. In fig. 3.7.1 three distributions with varying definitions for the induction time are visualized.

The three methods explicitly used here are given by the following:

Horizon crossing

The time of nucleation is obtained by following the trajectory of the largest cluster within a nucleated system back to the point where it last crossed the average largest cluster of the metastable fluid. The name horizon crossing refers to the idea that fluctuations of the

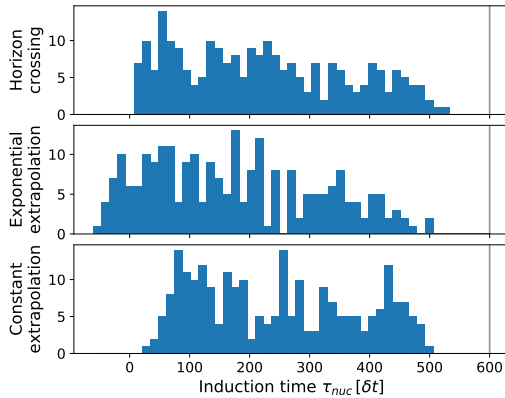


Figure 3.7.1.: Induction time distribution obtained by different definitions. While the two methods using extrapolation seem to have the two effects of smearing the signal as well as shifting them, the method of defining the nucleation as the time when the largest cluster is last below the horizon of fluctuations seems to return the most accurate and precise distribution. The final simulation time is marked by the grey line. As clusters require some time to clearly be recognized as crystals, no nucleation events can be observed towards the end of the simulation interval. To counteract this, we truncate the distribution in the analysis in such a way that it does not introduce a bias on the final result.

largest cluster are mostly independent, as the largest cluster is not fixed in the box but fluctuations at different locations contribute to it. Only extraordinary large fluctuations will be seen for prolonged periods of time and therefore will lead to correlated fluctuations of the largest cluster size. Thus, the name reflects the crossing of the trajectory below this horizon under which it does not describe a distinct cluster anymore.

Exponential extrapolation

For this method an exponential growth is fitted to the largest cluster data up to $N < 500$. Extrapolating to smaller times makes it possible to evaluate when the exponential function falls below 10 particles, which is then taken as the induction time. The method tends to find negative induction times that are not physical but only an artifact of the method.

Constant extrapolation

The name refers to the constant attachment rate found at later times for the cluster growth. It can be extrapolated to earlier times until the cluster completely vanishes. As the constant attachment rate is higher than the initial growth rate, this method returns too large induction times.

As it can be seen, the horizon crossing method returns a rather smooth distribution that can also roughly be approximated by an exponential decay that is expected for a constant nucleation rate as it is shown in section 3.8.1.

3.8. Induction time by exponential distribution assumption

As highlighted in section 1.6, induction times in simulation studies are often defined by the mean waiting time before nucleation is observed. This definition is rather unsuited at low volume fractions where induction times increase steeply, as it requires the theorist to wait until all simulation boxes showed nucleation. Therefore, we define the nucleation rate in the following without requiring complete crystallization. In fact, we also show that the statistical uncertainty of the induction time is not significantly reduced for measurements longer than the mean induction time.

3.8.1. CNT expectation of the induction time distribution

In section 1.4, we introduced classical nucleation theory and its constant nucleation rate depending on the barrier height in the free energy landscape. Even if there are signs that CNT is not appropriate for describing nucleation process completely, we will use its prediction of a constant nucleation rate as an assumption to define a constant scalar nucleation rate as well as comparing it to other literature values.

As mentioned before, in the discussion of the system sizes (section 3.1), the induction time of a system depends on the volume under consideration and for this reason it is commonly defined as a nucleation rate density κ . By also using the diffusion time $\tau_L = D_L^{-1}$ as a unit of time, the comparison to other systems with faster or slower dynamics is possible.

Considering a set of m simulations at a given volume fraction, we can describe the total system as a sum of m subvolumes, each of size V_{box} . Further, we can define the number of boxes in which a nucleation occurred as $n(t)$ and exclude them from the further simulation. In this case, the total nucleation rate \dot{n} can be written by eq. 3.8.1.

$$\dot{n} = (m - n(t))V_{\text{box}}k \quad (3.8.1)$$

$$\Leftrightarrow \frac{\dot{n}}{m} = \left(1 - \frac{n(t)}{m}\right)V_{\text{box}}k \quad (3.8.2)$$

Moreover, taking the continuous limit $m \rightarrow \infty$ and defining $\tau = (V_{\text{box}}k)^{-1}$, we can solve the differential equation to find the expected induction rate.

$$\Leftrightarrow \frac{n(t)}{m} = 1 - \exp\left(-\frac{t}{\tau}\right) \quad (3.8.3)$$

$$\Leftrightarrow \frac{\dot{n}(t)}{m} = \frac{1}{\tau} \exp\left(\frac{-t}{\tau}\right) \quad (3.8.4)$$

The final result in eq. 3.8.4 is the well known stochastic exponential distribution. As the expec-

tation value of the exponential distribution is given by its parameter τ , the common approach of using the mean induction time when all simulations have nucleated yields an accurate result and precision can be obtained by taking a large number of simulations.

3.8.2. Maximum likelihood estimator of the induction time

In case the simulation time is not accessible, we instead will have to deal with censored exponential distributions. For this, we can use maximum likelihood (ML) estimators. The derivation follows the one by Deemer and Votaw 1955[33].

Maximum likelihood estimators are based on the idea that we can write down the expression of the total probability, called likelihood \mathcal{L} , for a given set of measurements x_i depending on the parameters of the assumed underlying distribution. For the exponential distribution, parameterized by the characteristic decay rate κ , it is given by

$$\mathcal{L}(\kappa) = \prod_{i=1}^N p(x_i) = \prod_{i=1}^N \kappa^N \exp(-\kappa x_i) . \quad (3.8.5)$$

We continue, by finding the maximum of this product. To simplify it and also to evade overflow problems on floating point machines, the logarithm of the likelihood is used and maximized yielding the same parameters because the logarithm is a monotonic function and thus does not shift the extrema.

The maximum probability is found by usual means of analysis executed in eq. 3.8.6 - eq. 3.8.9.

$$0 \stackrel{!}{=} \frac{\partial \log(\mathcal{L})}{\partial \kappa} \Big|_{\kappa=\hat{\kappa}} \quad (3.8.6)$$

$$\Leftrightarrow 0 = \frac{\partial}{\partial \kappa} \left(N \log(\kappa) - \kappa \sum_{i=1}^N t_i \right) \Big|_{\kappa=\hat{\kappa}} \quad (3.8.7)$$

$$\Leftrightarrow 0 = \frac{N}{\hat{\kappa}} - \sum_{i=1}^N t_i \quad (3.8.8)$$

$$\Leftrightarrow \hat{\kappa}^{-1} = \frac{1}{N} \sum_{i=1}^N t_i \quad (3.8.9)$$

Through this, we have found that the maximum likelihood estimator of κ , for a set of samples drawn from an exponential distribution, is given by the inverse arithmetic mean of the samples. This result is neither new nor surprising but is shown to illustrate how the method of maximum likelihood works. In the following, we then show how to handle censored and truncated distributions by the maximum likelihood method.

Both distributions refer to sets of samples that are incomplete in the sense that they only include samples up to some threshold $t_i < T$. In the case of truncated distributions, the number of samples larger than this threshold is unknown. For the censored distribution, however, it is known. Taking the example of time consuming nucleation events in computer simulations, we are in the case of censored distributions, as the total number of boxes is known but the simulation is just stopped at some point without all boxes having had a nucleation event. The probability of an event later than the censoring time T is given by

$$p(t_i > T) = \int_T^\infty \kappa \exp(-\kappa t) dt = \exp(-\kappa T). \quad (3.8.10)$$

Therefore, we can write the complete probability distribution as

$$f(t) = \begin{cases} \kappa \exp(-\kappa t) & t < T \\ \exp(-\kappa T) & t \geq T \end{cases}. \quad (3.8.11)$$

In the simulation, we can then split up the number of boxes N into n boxes where a nucleation event was found and $m = N - n$ boxes without nucleation event during the simulation time T . Further, we have to account for the fact that the samples without distinct times are indistinguishable. This is done by weighting them with the number of possible permutations which are calculated in the binomial prefactor $\binom{N}{m}$. The whole expression for the likelihood function $\mathcal{L}(\kappa)$ then is given by eq. 3.8.12 and the extremum of it is evaluated in the subsequent reformulations.

$$\mathcal{L}(\kappa) = \binom{N}{m} \kappa^n \exp(-\kappa \sum_{i=1}^n t_i) \exp(-\kappa T)^m \quad \left| \frac{\partial \log(\dots)}{\partial \kappa} \right|_{\kappa=\hat{\kappa}} \quad (3.8.12)$$

$$\Leftrightarrow \log(\mathcal{L}(\kappa)) = \log \binom{N}{m} + n \log(\kappa) - \kappa \sum_{i=1}^n t_i - m \kappa T \quad \left| \frac{\partial(\dots)}{\partial \kappa} \right|_{\kappa=\hat{\kappa}} \quad (3.8.13)$$

$$\Leftrightarrow \frac{\partial \log(\mathcal{L}(\kappa))}{\partial \kappa} = \frac{n}{\kappa} - \sum_{i=1}^n t_i - mT \quad \left|_{\kappa=\hat{\kappa}} \quad (3.8.14)$$

$$\left. \quad \left| \quad \text{with } \frac{\partial \log(\mathcal{L}(\hat{\kappa}))}{\partial \kappa} \stackrel{!}{=} 0 \right. \right. \quad (3.8.15)$$

$$\Leftrightarrow 0 = \frac{n}{\hat{\kappa}} - \sum_{i=1}^n t_i - mT \quad (3.8.15)$$

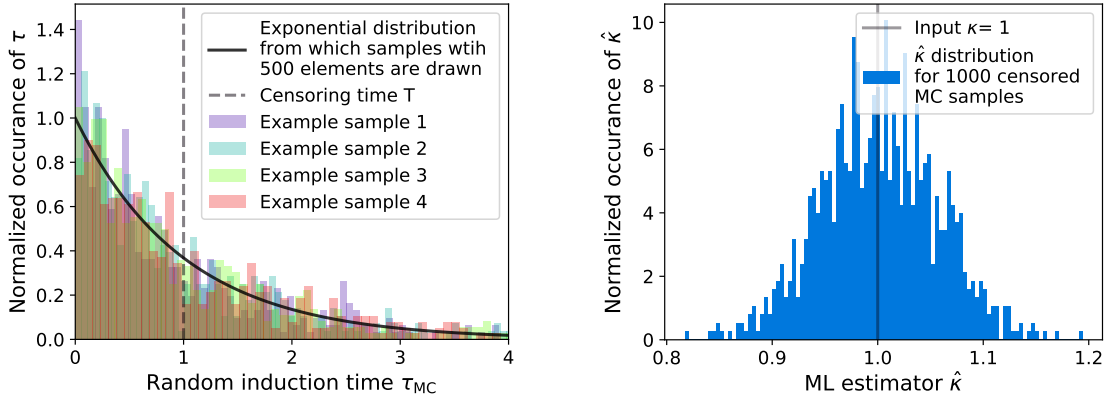
$$\Leftrightarrow \hat{\kappa}^{-1} = \frac{1}{n} \left(\sum_{i=1}^n t_i + mT \right) \quad (3.8.16)$$

The final line eq. 3.8.16 is the estimator of the decay rate of the censored exponential distribution. It is used for the estimation of induction times to compare with other published results in the next sections.

3.8.3. Monte Carlo uncertainty estimation

Having determined the estimator for the nucleation rate, the next question concerns its uncertainty i.e what is the distribution of $\hat{\kappa}$? While corresponding literature on analytic expressions for the distribution has been published for example by Chen and Bhattacharyya 1988[34], the complexity becomes inappropriate for the task at hand. Thus, we will follow instead a Monte Carlo approach as described in the book Numerical Recipes[35] to find the uncertainty of the estimator.

For this purpose, we draw samples from an exponential distribution characterized by the estimator calculated from the actual simulation data. Afterwards, the samples are censored by cutting off all elements larger than T and calculating the corresponding estimator $\hat{\kappa}_{MC}$ for the Monte Carlo sample. From multiple such random sets we can create a histogram of estimates for $\hat{\kappa}$ that can be seen together with some exemplary random samples in fig.3.8.1. As the distribution seems to incorporate only little higher moments, the standard deviation of the distribution is used as the estimators uncertainty $\sigma_{\hat{\kappa}}$.



(a) Exponentially distributed random samples of size 500 with an exemplary censoring time of $T = \kappa^{-1}$

(b) Distribution of $\hat{\kappa}$ for the previously generated MC samples. The distribution can be described mostly by mean and standard deviation as the number of estimates in the tails are small.

Figure 3.8.1.: Exemplary samples for a given κ as well as the distribution of estimates calculated from the random samples. The uncertainty on $\hat{\kappa}$ is approximated by the standard deviation of the distribution from the corresponding Monte Carlo analysis at a given κ .

Concerning the uncertainty in detail, we can ask how long a simulation should last to yield precise results. For this, we can first look at the case where $1 \gg \kappa T$ corresponding to a simulation where all boxes showed a nucleation event. In this case we have seen before that $\hat{\kappa}^{-1} = \frac{1}{N} \sum_{i=1}^N t_i$. As

we assume that t_i is exponentially distributed, we know that its standard deviation is given by $\sigma_t = \kappa^{-1}$. Gaussian error propagation then results in

$$\frac{\sigma_{\hat{\kappa}}}{\hat{\kappa}} = \frac{1}{\sqrt{N}} . \quad (3.8.17)$$

Similarly, we can take the limit of $1 \ll \kappa T$ which is the case when the mean nucleation time is much larger than the simulation time and, therefore, only a small fraction of the boxes hosted a nucleation event. In this case we can expand the estimator in the fraction of nucleated trajectories $\frac{n}{N}$ to find $\hat{\kappa} \approx \frac{n}{NT} \frac{1}{\kappa}$. In this limit, the gradient of the nucleation distribution is not seen and the rate is determined only by the fraction of boxes with a nucleation event. With n being Poisson distributed, we know that its standard deviation is given by $\sigma_n = \sqrt{n}$. Fixing N and T and using the expectation value of nucleations $n = N\hat{\kappa}T$, the Gaussian error propagation for the relative uncertainty is given by

$$\frac{\sigma_{\hat{\kappa}}}{\hat{\kappa}} = \frac{1}{\hat{\kappa}} \frac{\sqrt{n}}{NT} = \frac{\sqrt{N\hat{\kappa}T}}{NT\hat{\kappa}} = \frac{1}{\sqrt{N\hat{\kappa}T}} . \quad (3.8.18)$$

Finally, we are also able to not only look at limits analytically, but also to approximate the relative uncertainty directly by means of the aforementioned Monte Carlo method. For this purpose, the same procedure as before is used. The number of elements per sample is set consistently with the actual number of used simulations to 500 and to achieve good precision on the uncertainty, the standard deviation of 1000 samples is used. To compare the analytically derived limits of the uncertainty with the Monte Carlo results, both are drawn into fig. 3.8.2.

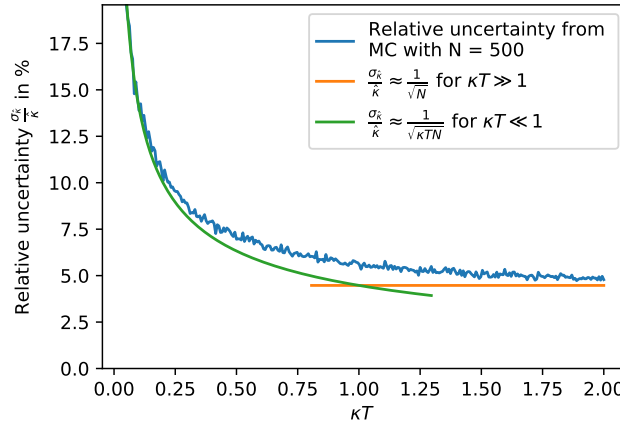


Figure 3.8.2.: Relative uncertainty of the ML estimator for varying κT . The x scale is chosen dimensionless such that it indicates the simulation time in comparison to the characteristic nucleation time.

As expected we find that, for the limits of $\kappa T \ll 1$ as well as $\kappa T \gg 1$, Monte Carlo and the analytical results are congruent, while in between only the Monte Carlo results can be used.

What can be seen from fig. 3.8.2 is that the uncertainty of the estimation drops sharply until about half of the characteristic induction time, after which it only obtains little more precision. This is not surprising, as the nucleation times contain the rate and more nucleation events occur at the beginning while long simulation times only add little further information. Thus, simulating until all boxes hosted a nucleation event is only necessary if one wants to use the simpler arithmetic mean of the induction times as the estimator, or if any other constraints make it necessary to reach crystallization of all boxes.

3.9. Nucleation rate discrepancy and possible solution

3.9.1. Comparison to literature

Finally, we are able to evaluate the induction time distribution to find the rates given in fig. 3.9.1.

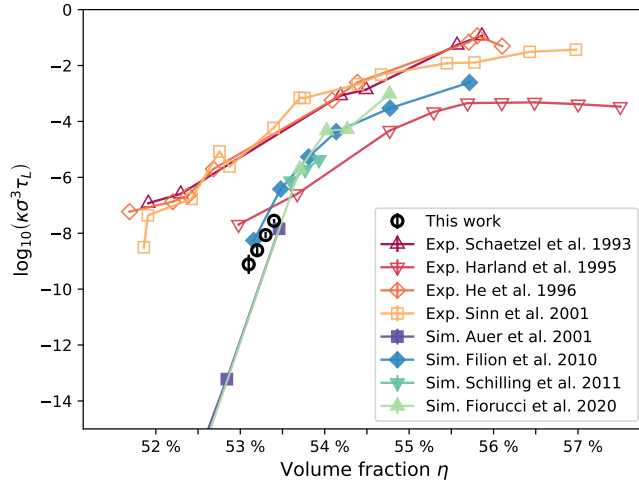


Figure 3.9.1.: Experimental and theoretical examples of nucleation rates in the hard sphere system at different volume fractions from the literature[7–9, 11, 36–39] to compare with the own measured data points. The values by Fiorucci et al. 2020 are depicted in units of the long time diffusion time, while in the publication the diffusion constant at infinite dilution D_0 is used. The change of units is done by using the measurement from section 2.2.1 and the definition $D_0 = \frac{3}{8\rho\sigma^2} \sqrt{\frac{k_B T}{m\pi}}$.

We can state that our measurements confirm the previous simulation results in a way that they still stand against the experimentally found ones from the diagram. Further, the results are calculated together with their statistical uncertainty, which is mostly visible for the data point at

$\eta = 53.1\%$. It is also indicated for the others but due to the logarithmic scaling the uncertainty is almost not visible.

While uncertainties in the literature are often just very roughly given, the here presented method makes it possible to quantify the statistical uncertainty of the rates and the large number of simulations leads to the high precision.

3.9.2. Solid fraction in the thermodynamic limit of infinite volume

In section 3.5, the cluster growth rate c is found to be mostly independent of the volume fraction in simulations. When extrapolating from the small region in which it was tested, we may approximate the number of particles N at time t for a cluster that emerged at time t_0 by

$$N(t) = c^3(t - t_0)^3 . \quad (3.9.1)$$

Furthermore, approximating the stochastic nucleation events with rate density κ by just adding a new cluster after every $\Delta t = (\kappa V)^{-1}$, we can write the total number of solidified particles N in a Volume V at time step m with the corresponding time $t_m = m\Delta t$ as the sum of all previously nucleated cluster sizes N_i . Reformulating leads to the final result in eq. 3.9.2.

$$\begin{aligned} N(t_m) &= \sum_{i=1}^m N_i & V \xrightarrow{\rightarrow \infty} \quad N(t) &= \kappa V \int_0^t c^3(t - t')^3 dt' \\ \Leftrightarrow N(t_m) &= \sum_{i=1}^m N_i \frac{\Delta t}{\Delta t} & \Leftrightarrow \frac{N(t)}{V \rho_{\text{melt}}} &= \frac{\kappa c^3}{\rho_{\text{melt}}} \frac{1}{4} t'^4 \Big|_{t''=0}^t \\ \Leftrightarrow N(t_m) &= \kappa V \sum_{i=1}^m N_i \Delta t & \Leftrightarrow \frac{V_{\text{solid}}}{V} &= t^4 \frac{\kappa c^3}{4 \rho_{\text{melt}}} \\ \Leftrightarrow N(t_m) &= \kappa V \sum_{i=1}^m c^3(t_m - t_i)^3 \Delta t & \Leftrightarrow x_s(t) &= t^4 \frac{\kappa c^3}{4 \rho_{\text{melt}}} \end{aligned} \quad (3.9.2)$$

Here, the solid fraction is not the equilibrium solid fraction but rather the expected solid fraction of an infinitely large system at a time t after some quench, that suddenly takes the system into the metastable regime.

For the derivation of eq. 3.9.2 the thermodynamic limit $V \rightarrow \infty$ is used to obtain the definition of an integral. Further, it neglects any interference between different clusters. This assumption is justified for $x_s \ll 1$ if no long range interference is present and heterogeneous nucleation is assumed to be part of the cluster growth process.

With this we can calculate a characteristic nucleation time t^* at which x_s is not negligible anymore. As in simulations with periodic boundary conditions clusters begin to interfere with

each other at a filling fraction of about $x_s = \frac{1}{8}$ which is also chosen as a threshold where interference can not be neglect any longer in the macroscopic system. Under this definition t^* becomes

$$t^* = \sqrt[4]{\frac{\rho_{\text{melt}}}{2\kappa c^3}}. \quad (3.9.3)$$

As we can see, the time t^* actually depends only on the fourth root of the induction time $\tau_{\text{nucleation}} = \kappa^{-1}$. This might be an explanation for the huge discrepancy between experiment and simulation studies, as can be seen in fig. 3.9.2, where the inverse of t^* is calculated from different simulation studies and depicted together with experimentally found nucleation rates.

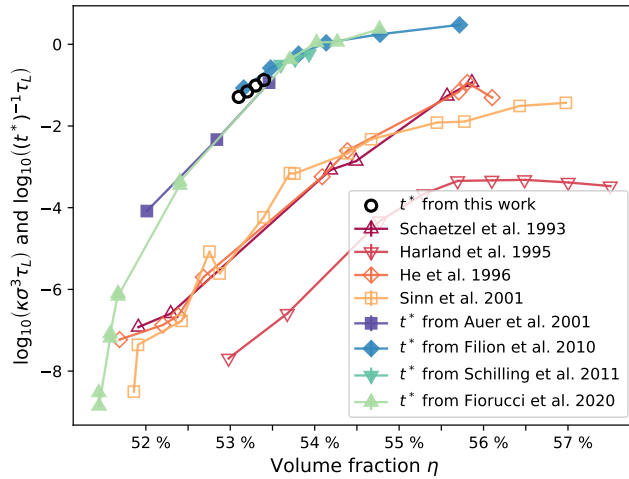


Figure 3.9.2.: Diagram with experimentally measured nucleation rates[7, 36–39] as well as $(t^*)^{-1}$ calculated from nucleation rates obtained in simulation studies[8, 9, 11]. The set of data points is equivalent to those of fig. 3.9.1.

What can be seen, is that the gradient of $(t^*)^{-1}$ calculated from the simulation studies follows mostly the one of the experimental results as the fourth root changes the slope by a factor of 4 in the logarithmic diagram. The rates still deviate by a factor of about 10000 which still requires explanation.

While this is not a proof, it might be a hint that laboratory based experiments measure more cluster growth than actual nucleation events. It has to be discussed with experimentalists if the assumptions leading to this result hold under closer inspection or if measures against this behavior have been taken.

3.10. Memory kernel analysis of nucleating ensemble

The approach by Hugues Meyer et al. 2019[4], to calculate memory kernels from an ensemble of trajectories, is used on the data discussed in the previous sections as well as on trajectories of a system characterized in tab. 3.10.1. The second system is used because the first ensemble was neither simulated up to the point where most boxes contained a stable cluster nor until the boxes were fully crystallized as the transition width is large and takes long simulations to fill up the box. The second system's parameters are chosen to fulfill both objections.

Parameter	Value
N	16384
eq. events/particle	5000
pr. events/particle	200000
η_i	45.0 %
η_f	53.4 %

Table 3.10.1.: Input parameters of simulations on the NEMO HPC cluster. The large number of production steps is chosen, together with the final volume fraction η_f , in a way to simulate nucleation and full crystallization of the boxes in almost all cases, as can be seen in the top diagram of fig. 3.10.1. Furthermore, the small box size leads to a small transition width Δ of about $150\delta t$ corresponding closely to the width of the memory kernel as lately shown by Meyer et al. 2021[40].

The memory kernel of the large system has been calculated but except for the Markovian contribution, only little was observed. This indicates that the sample is not sufficiently long or that the largest cluster is not an appropriate observable for quantifying nucleations in large systems.

To compare the memory kernel of the smaller system with direct measurements, the evolution of the largest cluster for the ensemble is depicted in the top of fig. 3.10.1. The trajectories have been normalized by the number of particles in the box and some statistical properties like percentiles and arithmetic mean are also shown, as the large number of trajectories otherwise makes it hard to distinguish the actual density of lines at some points. At the bottom of the figure, the share of trajectories at different stages of the nucleation process is identified. For this, it is assumed that those below a normalized largest cluster of 0.1 can be identified as not nucleated. Such trajectories above 0.5 are considered as fully crystallized and all of them in between as in the process of crystallization.

While in the large system only little of the crystallites reach the box boundaries, it can be observed that in the smaller system almost all clusters fill the whole box at the end of the simulation.

Further, as there is no clear analysis yet on how the direct quantities and the memory kernel

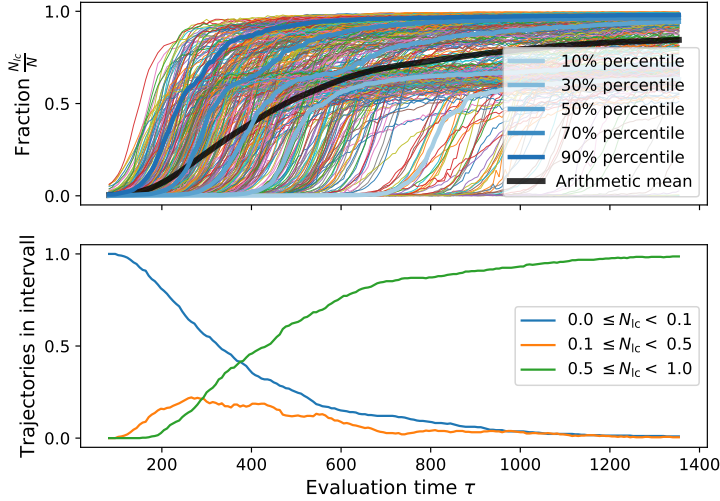


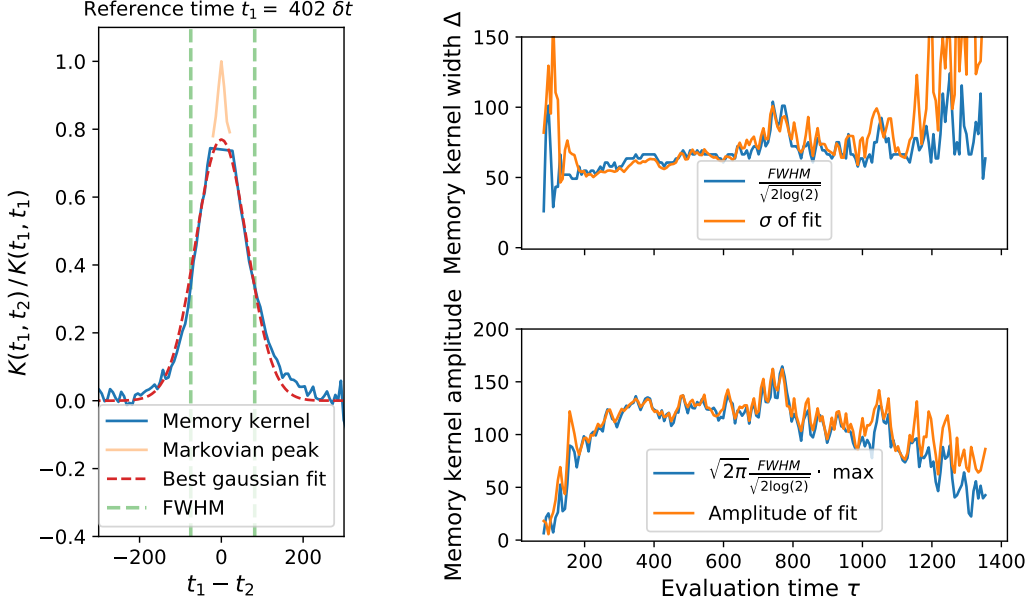
Figure 3.10.1.: Top: Normalized trajectories of largest cluster with percentiles and arithmetic mean indicated. It can be observed that some trajectories nucleate in more than one step. At first only about 60% of the box is filled by the crystal and at later times they may crystallize completely. From eq. 1.3.6 we would expect an equilibrium solid fraction of 80% by volume, closely corresponding to the expected solid fraction by particles.

Bottom: Fraction of trajectories within intervals chosen to identify nucleated trajectories, momentary growing trajectories and fully nucleated trajectories. As the transition is much faster than the distribution of nucleations, the orange curve roughly resembles the derivative of the other two curves.

are related, the subdivision is an approach to show direct observables that are possibly related to properties of the memory kernel.

We see on the left side of fig. 3.10.2, that the shape of a memory kernel slice at some reference time is rather simple. For this reason, we use a Gaussian fit to approximate the width and amplitude of the kernel. For this purpose, we neglect the Markovian part of the kernel at around $t_1 - t_2 \approx 0$. To validate the fit results, we further use the FWHM, with the maximum being determined by the mean value of the peak's crest. As the properly normalized results for both methods are in good agreement, we can conclude that the shape of the memory kernel in this case is mostly defined by a width and an amplitude over time, which are depicted on the right of fig. 3.10.2.

The width of the memory kernel sections are mostly constant over the whole measurement with the exception that it becomes very noisy at the end. The amplitude in comparison increases at the beginning, remains over a prolonged period of time constant and then declines towards the end of the measurement.



(a) Slice through memory kernel at the given reference time. The Markovian part is excluded from the analysis of the kernel width, that is depicted by the full width at half maximum (FWHM) and the Gaussian best fit. The FWHM is normalized to the value of a corresponding Gaussian curve.

(b) Top: Width of the memory kernel slices from FWHM and Gaussian fit. The FWHM is normalized to the value of a corresponding Gaussian curve. Bottom: Amplitude of the memory kernel slice on the one hand by using the mean value of the data around the maximum and on the other hand by using the amplitude derived from the best Gaussian fit. The amplitude derived from the maximum value is normalized to the value of a corresponding Gaussian curve.

Figure 3.10.2.: Example memory kernel together with width and amplitude depending on time.

As published by Meyer et al. 2021[40], the width of the memory kernel seems to depend on the phase transition time. However, the dependence does not seem related to the dynamics of the system because it is determined by the arbitrarily chosen box size. To separate the different memory effects, one could generate trajectories with a purely Markovian approach, like Brownian dynamics, with corresponding characteristic properties. Then, comparing the memory kernels of the purely Markovian ensemble with the a priori non-Markovian hard sphere ensemble may help to distinguish memory effects due to the system size from those related to the dynamics of the fluid.

Another approach would be to use the committer probability of the largest cluster as an observable, as it would not include a direct system size dependence and by itself is already bounded between zero and one, which is a requirement for the memory kernel analysis.

4. Conclusion

In the thesis at hand, the hard sphere nucleation process is studied. The current research topics it thereby addresses are the discrepancy between experimental and theoretical nucleation rates as well as the question if non-Markovian effects are present in the process. An EDMD simulation code that was developed for this purpose during the course of the year is presented together with a thorough testing and extensions for future studies. With the program, large data sets have been produced and characterized in detail.

First, we measure the long time self-diffusion constant in the metastable hard sphere fluid, as it is necessary to compare the timescale of the system.

Secondly, we semi-quantitatively find the duration in which the metastable clusters in the fluid find their ordering in three different contexts: The initial ordering process after the quench is visible in the cluster size distributions (section 3.3). Then, in the decay time of the autocovariance functions calculated from the largest cluster in the metastable fluid, we see the correlation time of large fluctuations, probably from distinct clusters (section 3.4). Finally, the duration is seen in direct measurements of the lifetimes of unstable clusters (section 2.5.2).

Third, the cluster growth and nucleation processes are investigated on. Regarding the growth process, we qualitatively look at shape descriptors derived from the tensor of gyration and try to find correlations between those and different scalar quantities characterizing the growth process. Even though, we do not find any correlations, we observe that clusters become more and more spherical up to a size of about 1000 particles after which they mostly grow without changing their proportions. The growth takes place with a constant attachment rate to the surface which varies between clusters by about 50%. Within the narrow interval in which the measurements are done, no dependence on the volume fraction is seen, but the statistical uncertainty does not exclude a dependence on the diffusion timescale.

Regarding the nucleation process, we discussed different definitions of the induction time and quantified the nucleation rate. To do so, we present a combination of the maximum likelihood estimator for censored exponential distributions and a robust Monte Carlo uncertainty estimation which then is employed. The results confirm the discrepancy between experimental and

theoretical rates that have been found in previous studies. Nevertheless, the detailed characterization leads us to a possible remedy but it requires further discussion with experimentalists and closer inspection.

Last but not least, we present the analysis of a two time memory kernel which has been calculated from trajectories of the largest cluster normalized by the total number of particles. For this purpose, a new ensemble of simulations is produced because the size of the one used to study the nucleation process is too large. The memory kernel on hand includes a Markovian and a non-Markovian contribution. The latter is well described by a Gaussian function of width comparable to the phase transition width of a single trajectory. The extent of the kernel is mostly constant over the whole time range. However, the amplitude increases at first, then remains constant and decreases when most trajectories are in the complete crystalline state. It probably will be necessary to address the question on how the here visible memory contribution depends on the arbitrary box size to reveal possible memory effects originating from the dynamics of the system.

A. Derivation of momentum transfer in elastic hard sphere collisions

The elastic collision of two hard spheres i and j is governed by energy and momentum conservation. In the collision of the two particles, the momentum transfer $\Delta\vec{p}$ is confined within the direction of relative position because the collision is instantaneous. Thus, we may write the momentum transfer on particle i as $\Delta\vec{p}_i = a\vec{r}_{ij}$ with the relative position $\vec{r}_{ij} = \vec{r}_j - \vec{r}_i$ and a being some constant to be determined. It can be easily seen that $\Delta\vec{p}_i = -\Delta\vec{p}_j$ due to $\vec{r}_{ij} = -\vec{r}_{ji}$.

Using $\vec{p}_i = m_i\vec{v}_i$, we can write the velocity after the collision for particle i as

$$\vec{v}'_i = \vec{v}_i + \frac{\Delta\vec{p}_i}{m_i}. \quad (\text{A.0.1})$$

By using classical energy conservation and reformulating, we find

$$\frac{1}{2} (m_i|\vec{v}_i|^2 + m_j|\vec{v}_j|^2) = \frac{1}{2} (m_i|\vec{v}'_i|^2 + m_j|\vec{v}'_j|^2) \quad (\text{A.0.2})$$

$$\Leftrightarrow m_i|\vec{v}_i|^2 + m_j|\vec{v}_j|^2 = m_i \left(\vec{v}_i + \frac{\Delta\vec{p}_i}{m_i} \right)^2 + m_j \left(\vec{v}_j + \frac{\Delta\vec{p}_j}{m_j} \right)^2 \quad (\text{A.0.3})$$

$$\Leftrightarrow 0 = 2(\vec{v}_i \cdot \Delta\vec{p}_i + \vec{v}_j \cdot \Delta\vec{p}_j) + \frac{|\Delta\vec{p}_i|^2}{m_i} + \frac{|\Delta\vec{p}_j|^2}{m_j} \quad (\text{A.0.4})$$

$$\Leftrightarrow 0 = 2(\vec{v}_i - \vec{v}_j) \cdot \Delta\vec{p}_i + |\Delta\vec{p}_i|^2 \left(\frac{1}{m_i} + \frac{1}{m_j} \right) \quad (\text{A.0.5})$$

$$\Leftrightarrow 2a\vec{r}_{ij} \cdot \vec{v}_{ij} = a^2|\vec{r}_{ij}|^2 \frac{m_i + m_j}{m_i m_j} \quad (\text{A.0.6})$$

$$\Leftrightarrow a = \frac{2m_i m_j}{(m_i + m_j)} \frac{\vec{r}_{ij} \cdot \vec{v}_{ij}}{|\vec{r}_{ij}|^2} \quad (\text{A.0.7})$$

$$\Rightarrow \vec{v}'_{i/j} = \vec{v}_{i/j} \pm \frac{2m_{j/i}}{(m_i + m_j)} \frac{\vec{r}_{ij} \cdot \vec{v}_{ij}}{|\vec{r}_{ij}|^2} \quad (\text{A.0.8})$$

Equation A.0.8, is the final result which is used in the thesis.

Acknowledgements

First of all, i want to thank Tanja Schilling for granting me a lot of freedom, while always hinting relevant details and for providing the large resources for the simulation study. Secondly, i want to thank Anja Kuhnbold for the short line of communication that helped solve many small questions. And then, i want to thank Hugues Meyer and Fabian Glatzel, as they elaborated and developed the theoretical and numerical base on which the memory kernel analysis relies.

Further, the author acknowledges support by the state of Baden-Württemberg through bwHPC and the German Research Foundation (DFG) through grant no INST 39/963-1 FUGG (bwFor-Cluster NEMO).

Bibliography

- ¹R. P. Sear, “The non-classical nucleation of crystals: microscopic mechanisms and applications to molecular crystals, ice and calcium carbonate”, International Materials Reviews **57**, 328–356 (2012).
- ²A. Kuhnhold et al., “Derivation of an exact, nonequilibrium framework for nucleation: Nucleation is a priori neither diffusive nor Markovian”, Physical Review E **100**, 52140 (2019).
- ³P. Pelagejcev, “Simulation study of non-Markovian effects in crystal nucleation”, Master Thesis (Albert-Ludwigs-Universität Freiburg, 2019).
- ⁴H. Meyer, P. Pelagejcev, and T. Schilling, “Non-Markovian out-of-equilibrium dynamics: A general numerical procedure to construct time-dependent memory kernels for coarse-grained observables”, EPL **128**, 40001 (2019).
- ⁵H. Meyer, “Generalized Langevin Equations and memory effects in non-equilibrium statistical physics”, Dissertation (Université du Luxembourg, Albert-Ludwigs-Universität Freiburg, 2020).
- ⁶H. Meyer, T. Voigtmann, and T. Schilling, “On the non-stationary generalized Langevin equation”, The Journal of Chemical Physics **147**, 214110 (2017).
- ⁷S. Auer and D. Frenkel, “Prediction of absolute crystal-nucleation rate in hard-sphere colloids”, Nature **409**, 1020–1023 (2001).
- ⁸L. Filion, M. Hermes, R. Ni, and M. Dijkstra, “Crystal nucleation of hard spheres using molecular dynamics, umbrella sampling, and forward flux sampling: A comparison of simulation techniques”, Journal of Chemical Physics **133**, 244115 (2010).
- ⁹T. Schilling, S. Dorosz, H. J. Schöpe, and G. Opletal, “Crystallization in suspensions of hard spheres: A Monte Carlo and molecular dynamics simulation study”, Journal of Physics Condensed Matter **23**, 194120 (2011).
- ¹⁰N. H. Wood, “Hard Sphere Nucleation Rates”, Dissertation (University of Bristol, 2019).
- ¹¹G. Fiorucci, G. M. Coli, J. T. Padding, and M. Dijkstra, “The effect of hydrodynamics on the crystal nucleation of nearly hard spheres”, Journal of Chemical Physics **152**, 064903 (2020).
- ¹²B. J. Alder and T. E. Wainwright, “Studies in Molecular Dynamics. I. General Method”, The Journal of Chemical Physics **31**, 459–466 (1959).

- ¹³A. Mulero, C. Galán, and F. Cuadros, “Equations of state for hard spheres. A review of accuracy and applications”, *Physical Chemistry Chemical Physics* **3**, 4991–4999 (2001).
- ¹⁴N. F. Carnahan and K. E. Starling, “Equation of state for nonattracting rigid spheres”, *The Journal of Chemical Physics* **51**, 635–636 (1969).
- ¹⁵N. G. Almarza, “A cluster algorithm for Monte Carlo simulation at constant pressure”, *Journal of Chemical Physics* **130**, 184106 (2009).
- ¹⁶R. Becker and W. Döring, “Kinetische Behandlung der Keimbildung in übersättigten Dämpfen”, *Annalen der Physik* **416**, 719–752 (1935).
- ¹⁷M. Bültmann and T. Schilling, “Computation of the solid-liquid interfacial free energy in hard spheres by means of thermodynamic integration”, *Physical Review E* **102**, 1–7 (2020).
- ¹⁸P. N. Pusey and W. van Megen, “Phase behaviour of concentrated suspensions of nearly colloidal spheres”, *Nature* **320**, 340–342 (1986).
- ¹⁹M. P. Doherty, C. T. Lant, and J. S. Ling, “The physics of hard spheres experiment on MSL-1: Required measurements and instrument performance”, in *36th aiaa aerospace sciences meeting and exhibit* (1998).
- ²⁰M. Radu and T. Schilling, “Solvent hydrodynamics speed up crystal nucleation in suspensions of hard spheres”, *Epl* **105**, 1–7 (2014).
- ²¹M. N. Bannerman, S. Strobl, A. Formella, and T. Pöschel, “Stable algorithm for event detection in event-driven particle dynamics”, *Computational Particle Mechanics* **1**, 191–198 (2014).
- ²²D. Goldberg, “What Every Computer Scientist Should Know About Floating-Point Arithmetic”, *ACM Comput. Surv.* **23**, 10 (1991).
- ²³M. N. Bannerman, R. Sargent, and L. Lue, “DynamO: A free O(N) general event-driven molecular dynamics simulator”, *Journal of Computational Chemistry* **32**, 3329–3338 (2011).
- ²⁴A. Donev, S. Torquato, and F. H. Stillinger, “Neighbor list collision-driven molecular dynamics simulation for nonspherical hard particles.II. Applications to ellipses and ellipsoids”, *Journal of Computational Physics* **202**, 765–793 (2005).
- ²⁵P. J. Steinhardt, D. R. Nelson, and M. Ronchetti, “Bond-orientational order in liquids and glasses”, *Physical Review B* **28**, 784–805 (1983).
- ²⁶P. R. Ten Wolde, M. J. Ruiz-Montero, and D. Frenkel, “Numerical evidence for bcc ordering at the surface of a critical fcc nucleus”, *Physical Review Letters* **75**, 2714–2717 (1995).
- ²⁷A. Einstein, “Über die von der molekularkinetischen Theorie der Wärme geforderte Bewegung von in ruhenden Flüssigkeiten suspendierten Teilchen”, *Annalen der Physik* **322**, 549–560 (1905).

- ²⁸S. Pieprzyk et al., “Thermodynamic and dynamical properties of the hard sphere system revisited by molecular dynamics simulation”, *Physical Chemistry Chemical Physics* **21**, 6886–6899 (2019).
- ²⁹D. M. Heyes, M. J. Cass, J. G. Powles, and W. A. Evans, “Self-diffusion coefficient of the hard-sphere fluid: System size dependence and empirical correlations”, *Journal of Physical Chemistry B* **111**, 1455–1464 (2007).
- ³⁰I. R. Hansen, Jean-Pierre McDonald, “Chapter 4 - Distribution-function Theories”, in *Theory of simple liquids*, Third Edit (Academic Press, 2006), p. 94.
- ³¹P. N. Pusey et al., “Hard spheres: crystallization and glass formation”, *Philosophical Transactions of the Royal Society A: Mathematical, Physical and Engineering Sciences* **367**, 4993–5011 (2009).
- ³²D. N. Theodorou and U. W. Suter, “Shape of Unperturbed Linear Polymers: Polypropylene”, *Macromolecules* **18**, 1206–1214 (1985).
- ³³W. L. Deemer and D. F. Votaw, “Estimation of Parameters of Truncated or Censored Exponential Distributions”, *The Annals of Mathematical Statistics* **26**, 498–504 (1955).
- ³⁴S. M. Chen and G. K. Bhattacharyya, “Exact confidence bounds for an exponential parameter under hybrid censoring”, *Communications in Statistics - Theory and Methods* **17**, 1857–1870 (1988).
- ³⁵W. H. Press, S. A. Teukolsky, W. T. Vetterling, and B. P. Flannery, “Confidence Limits on Estimated Model Parameters”, in *Numerical recipes in fortran 77: the art of scientific computing*, 2nd ed. (Cambridge University Press, 1992) Chap. 15, pp. 684–686.
- ³⁶J. L. Harland and W. van Megen, “Crystallization kinetics of suspensions of hard colloidal spheres”, *Physical Review E* **55**, 3054–3067 (1997).
- ³⁷Y. He et al., “Dynamics of crystallization in hard-sphere suspensions”, *Physical Review E* **54**, 5286–5297 (1996).
- ³⁸K. Schätzel and B. J. Ackerson, “Density fluctuations during crystallization of colloids”, *Physical Review E* **48**, 3766–3777 (1993).
- ³⁹C. Sinn, A. Heymann, A. Stipp, and T. Palberg, “Solidification kinetics of hard-sphere colloidal suspensions”, *Trends in Colloid and Interface Science XV. Progress in Colloid and Polymer Science* **118**, 266–275 (2001).
- ⁴⁰H. Meyer, F. Glatzel, W. Wöhler, and T. Schilling, “Evaluation of memory effects at phase transitions and during relaxation processes”, *Physical Review E* **103**, 22102 (2021).

